

MATHEMATICAL MODELING OF SOLIDIFICATION PHENOMENA IN
ELECTROMAGNETICALLY STIRRED MELTS

by

GREGORY MICHAEL POOLE

LAURENTIU NASTAC, COMMITTEE CHAIR

MARK L. WEAVER

HEATH TURNER

AMBER GENAU

CHARLES A. MONROE

A DISSERTATION

Submitted in partial fulfillment of the requirements
for the degree of Doctor of Philosophy in the
Department of Metallurgical and Materials Engineering
in the Graduate School of
The University of Alabama

TUSCALOOSA, ALABAMA

2014

Copyright Gregory Michael Poole 2014
ALL RIGHTS RESERVED

ABSTRACT

A methodology is presented to simulate the electromagnetic, heat transfer, and fluid flow phenomena for two dimensional electromagnetic solidification processes. For computation of the electromagnetic field, the model utilizes the mutual inductance technique to limit the solution domain to the molten metal and magnetic shields, commonly present in solidification systems. The temperature and velocity fields were solved using the control volume method in the metal domain. The developed model employs a two domain formulation for the mushy zone. Mathematical formulations are presented for turbulent flow in the bulk liquid and the suspended particle region, along with rheological behavior. An expression has been developed—for the first time—to describe damping of the flow in the suspended particle region as a result of the interactions between the particles and the turbulent eddies. The flow in the fixed particle region is described using Darcy's law. Calculations were carried out for globular and dendritic solidification morphologies of an electromagnetically-stirred melt in a bottom-chill mold. The coherency solid fraction for the globular solidification morphology was taken to be 0.5, while the coherency for dendritic morphology was 0.25. The results showed the flow intensity in the suspended particle region was reduced by an order of magnitude. The effect of the heat extraction rate on solidification time was investigated using three different heat transfer coefficients. The results showed that the decrease in solidification time is nonlinear with respect to increasing heat transfer coefficient. The influence of the final grain size on the damping of the

flow in the suspended particle region was examined, and it was found that larger grain sizes reduce the extent of flow damping.

LIST OF ABBREVIATIONS AND SYMBOLS

A Magnetic vector potential

B Magnetic flux density

C_1^* Turbulence constant

C_2^* Turbulence constant

C_μ^* Drag coefficient

C_L Liquid concentration

C_S Solid concentration

C^* Apparent heat capacity

c_d Damping force constant

c_p Specific heat

$c_{p,l}$ Liquid specific heat

$c_{p,s}$ Solid specific heat

D_g Final grain size

| | |
|-------------------|----------------------------|
| D_L | Mass diffusivity of liquid |
| D_m | Molecular mass diffusivity |
| d | Instantaneous grain size |
| $d\mathbf{l}$ | Differential line element |
| \mathbf{E} | Electric field |
| EM | Electromagnetic |
| \mathbf{F}_b | Bouyancy force |
| \mathbf{F}_{em} | Lorentz force |
| \mathbf{F}_d | Damping force |
| f_c | Coherency solid fraction |
| f_l | Liquid fraction |
| f_s | Solid fraction |
| G_{ij} | Turbulent shear generation |
| I_k | Coil current |
| I_T | Turbulent intensity |
| \mathbf{J} | Current density vector |
| j | Square root of -1 |

| | |
|---------------|------------------------------------|
| K | Flow permeability |
| k | Turbulent kinetic energy |
| k^* | Effective thermal conductivity |
| k_s | Thermal conductivity of the solid |
| k_l | Thermal conductivity of the liquid |
| L | Latent heat of fusion |
| M_{ij} | Mutual inductance |
| \mathbf{n} | Unit surface normal |
| P | Pressure |
| Pr | Prandtl number |
| \mathbf{r} | Position vector |
| \mathbf{r}' | Source position vector |
| R | Radius of metal specimen |
| R_T | Turbulent Reynolds number |
| \mathbf{S} | Surface normal |
| Sc | Schmidt number |
| S_{em} | Electrical energy dissipation |

| | |
|---------------|-----------------------------------|
| T | Temperature |
| T_L | Liquidus temperature |
| T_S | Solidus temperature |
| t | Time |
| \mathbf{u} | Velocity vector |
| u' | Turbulent fluctuating velocity |
| V | Volume, Electric scalar potential |
| ∇ | Del operator |
| β | Particle-to-envelope volume ratio |
| δ_{ij} | Kronecker delta |
| ε | Turbulent energy dissipation |
| λ | Switching parameter |
| ρ | Density |
| μ | Viscosity |
| μ_0 | Permeability of free space |
| μ_m | Molecular viscosity |
| μ_l | Laminar viscosity |

| | |
|----------------------|--|
| μ_t | Turbulent viscosity |
| σ | Electrical conductivity |
| σ_k | Turbulent Prandtl number for k |
| σ_ε | Turbulent Prandtl number for ε |
| τ_t | Turbulent (Reynolds) Stress |
| ψ | Magnetic scalar potential |
| ϕ | Reduced electric scalar potential |
| ω | Angular frequency |
| Ω | Solute generation source term |

ACKNOWLEDGEMENTS

When I began composing this dissertation, I would have never imagined that I would complete my studies without a man who, in the end, not only guided me in my acquisition of knowledge, but also became a dear friend. Professor Nagy El-Kaddah was a the best person I could have ever asked for in a research advisor. He and I would not only discuss the fundamental phenomena that governs the world in which we live, but would also delve into the very heart of issues of philosophy and the human condition. I cannot imagine where I would be today had he not mentored me in both my undergraduate years as a student and later as his pupil, and I only hope to be half of the mentor he was to me to others. Unfortunately, his time was cut short, and his no longer being among us is a tragedy of the greatest kind. Both the University of Alabama and I will greatly miss him.

I would first like to express my gratitude to my other advisor, Dr. Laurentiu Nastac, who took the reins amidst a difficult situation and guided me to further my career goals. I would also like to thank the National Science Foundation for affording the great privilege to complete this work under grant number CMMI-0856320. I would also like thank the members of my defense committee, Drs. Mark L. Weaver, Heath Turner, Amber Genau and Charles A. Monroe for taking the time to offer their insights and suggestions on this project.

In addition to those who have been instrumental in directly offering their guidance in this work, prudence dictates that gratitude be expressed for those who have made indelible impressions on my career. Professor David Nikles has been my greatest supporter at the University of Alabama, beginning with my interning in his research lab within the Center for Materials for Information Technology developing magnetic data storage materials—an

internship that led me to devote my learning and explaining the world around us to others. I would also like to thank my high school mathematics teachers, Ms. Vanetta Clark, Mrs. Betty Trayvick, Mrs. Susan Copen, and Mrs. Elaine Noland, whose instruction inspired me to gain and apply my mathematical knowledge to the benefit of others. Most importantly, I thank my father, Michael, and my mother, Susan, for supporting my endless quest for knowledge, and for their constant consolation and encouragement along the way.

Finally, I must acknowledge the pillar and foundation of truth, whose truth I am merely rediscovering—*Veritas Christo et Ecclesiae*.

CONTENTS

| | |
|--|-----|
| ABSTRACT..... | ii |
| LIST OF ABBREVIATIONS AND SYMBOLS | iii |
| ACKNOWLEDGEMENTS | ix |
| LIST OF TABLES | xiv |
| LIST OF FIGURES | xv |
| Chapter 1. Introduction | 1 |
| Chapter 2. Literature Review | 7 |
| 2.1 Computational Electromagnetics | 7 |
| 2.2 Modeling of Heat Transfer during Solidification | 11 |
| 2.2.1 Isothermal Solidification..... | 12 |
| 2.2.2 Solidification of Alloys..... | 12 |
| 2.3 Modeling of Fluid Flow during Solidification..... | 15 |
| 2.3.1 Single-zone Models | 17 |
| 2.3.2 Dual-zone Models | 19 |
| 2.4 Modeling of Solute Segregation during Solidification | 21 |
| Chapter 3. An Improved Model for the Flow in an Electromagnetically Stirred Melt during Solidification..... | 24 |
| 3.1 Abstract..... | 24 |
| 3.2 Introduction..... | 24 |
| 3.3 Model Formulation | 26 |

| | |
|--|----|
| 3.3.1 Electromagnetic Field | 27 |
| 3.3.2 Heat Transfer | 28 |
| 3.3.3 Fluid Flow | 29 |
| 3.3.4 Turbulent Damping Model | 28 |
| 3.4 Solution Technique | 32 |
| 3.5 Results and Discussion | 33 |
| 3.6 Conclusions..... | 43 |
| 3.7 Acknowledgements..... | 45 |
| 3.8 References..... | 45 |
| Appendix 3A: The Damping Force in the Suspended Particle Region | 48 |
| Chapter 4. The Effect of Coil Design on the Temperature and Velocity Fields during Solidification in Electromagnetic Stirring Processes | 49 |
| 4.1 Abstract..... | 49 |
| 4.2 Introduction..... | 50 |
| 4.3 Model Formulation | 51 |
| 4.3.1 Formulation of the Electromagnetic Field Problem..... | 52 |
| 4.3.2 Formulation of the Heat Transfer Problem..... | 53 |
| 4.3.3 Formulation of the Fluid Flow Problem | 54 |
| 4.3.4 Turbulent Damping Model | 55 |
| 4.4. Solution Technique | 56 |
| 4.5 Results and Discussion | 57 |
| 4.6 Conclusions..... | 65 |
| 4.7 References..... | 66 |

| | |
|---|----|
| Chapter 5. Numerical Modeling of Macrosegregation in Al-Cu Alloys Solidifying in the Presence of Electromagnetic Stirring..... | 68 |
| 5.1 Abstract..... | 68 |
| 5.2 Introduction..... | 68 |
| 5.3 Model Formulation | 70 |
| 5.3.1 Electromagnetic Field | 71 |
| 5.3.2 Fluid Flow | 71 |
| 5.3.3 Heat Transfer | 73 |
| 5.3.4 Solute Segregation | 74 |
| 5.4 Results and Discussion | 75 |
| 5.4.1 Computed Results | 76 |
| 5.4.2 Comparison with Experimental Measurements | 81 |
| 5.4.3 Influence of Various Parameters..... | 83 |
| 5.5 Conclusions..... | 86 |
| 5.6 References..... | 87 |
| Chapter 6. Conclusions and Future Work..... | 91 |
| 6.1 Concluding Remarks..... | 91 |
| 6.2 Recommendations for Future Research | 92 |
| References..... | 92 |

LIST OF TABLES

| | |
|---|----|
| 3.1 Thermophysical properties of Al-4.5%Cu alloy | 33 |
| 5.1 Thermophysical properties used in the present study | 74 |

LIST OF FIGURES

| | |
|---|----|
| 3.1 Sketch of a typical EM stirred solidification system | 25 |
| 3.2 Flow domains for the dual-zone solidification model | 28 |
| 3.3 Dimensions of the system used in this study | 32 |
| 3.4 Computed Lorentz (EM) force field in the metal and chill block..... | 34 |
| 3.5 Computed vorticity of the EM force field in the metal..... | 35 |
| 3.6 Initial characteristics of the flow: (a) velocity and (b) turbulent-to-laminar viscosity ratio..... | 36 |
| 3.7 Computed velocity profiles in the metal at: (a) 30s, (b) 60s, (c) 120s, (d) 240s. Contours correspond to values of solid fraction..... | 37 |
| 3.8 Computed turbulent-to-laminar viscosity in the metal at: (a) 30s, (b) 60s, (c) 120s, (d) 240s..... | 39 |
| 3.9 Comparison between the velocity in the suspended particle region with and without damping force | 40 |
| 3.10 Comparison of turbulence in the suspended particle region with and without damping force | 41 |
| 3.11 Influence of final grain size, D_g , on damping of velocity in the suspended particle region..... | 41 |
| 3.12 Influence of final grain size, D_g , on damping of turbulence in the suspended particle region..... | 42 |
| 4.1 Sketch of unidirectional EM solidification system..... | 56 |
| 4.2 Initial flow patterns at different coil locations: (a) middle, (b) top, and (c) bottom..... | 58 |
| 4.3 Initial turbulent fields at different coil positions: (a) middle, (b) top, and (c) bottom..... | 59 |
| 4.4 Computed velocity and temperature fields in the suspended particle region after 120s: (a) middle, (b) top, and (c) bottom coil positions..... | 61 |
| 4.5 A comparison of the radial temperature distributions for the top and bottom coil positions after 120s ($z=20$ mm)..... | 62 |

| | |
|---|----|
| 4.6 Decay of velocity in the suspended particle region for top and bottom coil positions (r=20 mm, z=30 mm) | 63 |
| 4.7 Decay of turbulent-to-laminar viscosity ratio in the suspended particle region for top and bottom coil positions (r=20 mm, z=30 mm) ... | 64 |
| 5.1 Flow domains for the dual-zone solidification model | 70 |
| 5.2 Dimensions of the system used in this study | 75 |
| 5.3 Initial computed velocity field | 75 |
| 5.4 Initial turbulent field given in terms of turbulent-to-molecular viscosity | 76 |
| 5.5 Damping of the velocity and turbulent fields. Data taken at the centerline 20 mm from the chill..... | 77 |
| 5.6 Computed velocity and liquid solute profile after 360s for frequency of 4900 Hz..... | 78 |
| 5.7 Solute segregation profile after 550s. Note the change of scale in the velocity..... | 79 |
| 5.8 Axial liquid concentration profiles, taken at the centerline for different stages of solidification..... | 80 |
| 5.9 Electron backscatter micrographs taken for EM stirred sample at (a) 20 mm and (b) 60 mm from chill block. Images taken at ingot centerline..... | 80 |
| 5.10 Final computed composition profiles at different radii compared with experimental measurements..... | 81 |
| 5.11 Influence of assumed f_s vs T profile on the final solute composition at the centerline | 82 |
| 5.12 Influence of final grain size on the final centerline composition..... | 83 |
| 5.13 Effect of frequency on centerline segregation | 84 |
| 5.14 Velocity and liquid solute concentration field after 360 seconds for frequency of 500 Hz..... | 84 |

Chapter 1

Introduction

In the past several decades, electromagnetic (EM) induction stirring technologies have become an attractive means to achieve a fine-grained equiaxed structure in solidification processes. In EM stirring, an alternating current is passed through a suitable induction coil; this, in turn, generates eddy currents within the molten metal. These eddy currents then interact with the time-varying magnetic field generated by the coil to generate stirring (Lorentz) forces, the rotational component of which drives the flow. This ability to produce an “action at a distance” by generating flows without any physical contact with the melt—often a cause of contamination—makes EM stirring uniquely useful in a number of solidification processes. To this end, examples of EM stirring being utilized during solidification include continuous casting [1-3], direct chill (DC) casting [4, 5], suspension melting [6, 7], and semiconductor processing using Bridgeman furnaces [8, 9].

In most cases, the flows generated by EM stirring are very intense and highly turbulent; this causes the convective phenomena in the melt to exert a dominating influence on the micro- and macrostructural evolution of the cast alloy, particularly in the early stages of solidification. The influences of EM stirring flows on the solidification are well-documented in the experimental literature and are manifold in scope. In the bulk liquid, the flow serves to promote homogeneous solute and temperature fields in the melt [10-12]. Furthermore, the flow causes the superheat in the melt to dissipate rapidly due to the increased Nusselt number near the chill interface, facilitating a greater nuclei survival probability [13] and uniform growth kinetics [14, 15]. As solidification commences and a two-phase “mushy” region forms, the flow continues to

minimize the temperature gradient between the solid crystallites and the surrounding liquid [16], promoting an earlier occurrence of the columnar-to-equiaxed transition in the cast alloy [17]. However, the greatest contribution of EM stirring to grain refinement comes via the dendrite fragmentation mechanism, first proposed by Jackson and co-workers [18] and confirmed through *in situ* experiments [19-21]. In dendrite fragmentation, flow between coalesced dendrites transports, or “washes”, solute-enriched liquid from deep within the mushy region to the solid-liquid interface. This causes the secondary dendrite arms at the interface to undergo remelting, and the detached tips are then carried into the liquid, increasing the nucleation potential of the melt and thus reducing the grain size.

In addition to micro- and macrostructural changes induced by EM stirring, the flow also has a profound effect on the distribution of solute in the mushy region, commonly referred to as “segregation”. Indeed, it has been repeatedly shown on the macroscale that, depending on the type of field used, the solute profiles within the solidified cast alloy vary greatly depending on the flow characteristics, which themselves depend on the type of magnetic field used, the most common of which are stationary [3, 22], rotating [23], and traveling magnetic fields [24]. On the microscale, the flow modifies the extent of solute rejection, represented by the partition coefficient [25].

This creates an imperative to understand the flow characteristics in both the melt and mushy regions in order to ensure adequate control of the solidification phenomena within the cast alloy. To this end, the development and implementation of mathematical modeling tools provides an attractive and economical alternative to incessant experimentation; however, these developed tools, while useful, are only as reliable if the physical phenomena that the model intends to reflect are well-defined. Therefore, it is vital that all aspects of electromagnetic, heat

transfer, fluid flow, and mass transfer phenomena in both the bulk liquid and mushy regions must be accounted for if a rigorous solution is to be obtained for any EM stirred solidification system.

Previous work, exemplified by those of Evans [26, 27], Szekely [21, 28], and El-Kaddah [29, 30], have led to a good fundamental understanding of the phenomena involved in EM stirring of bulk liquids. Their approach involves the solution of the Maxwell equations for the electromagnetic field and the turbulent Navier-Stokes equations in the bulk liquid. However, implementation of the methods described in the references above becomes more cumbersome when considering two-phase flows.

There have been a number of approaches developed to describe the flow in the mushy region. Initial efforts involved treating the mushy region as a porous medium governed by Darcy's law [31-34], along with supplementary relations for describing the flow permeability [35, 36]. It is important to note that these models, which assume stationary crystallites, are only suitable to either laminar buoyancy-driven or shrinkage-driven flows during; however, there have been some efforts to incorporate turbulent flow behavior [37, 38]. Furthermore, such flows are physically valid for columnar solidification only, as equiaxed grains travel with the flow at low fraction solid [18-20].

To remedy this, a new model, introduced by Oldenburg and Spera [39], relaxes the porous medium assumption at low fraction solid, replacing it with a homogeneous two-phase flow formulation where the viscosity of the solid-liquid mixture is described by rheological behavior. The Darcy flow assumption is maintained at higher fraction solid, with the two flow domains being delineated by the coherency fraction solid, defined as when the growing crystallites first begin to impinge on one another. Other variations of the dual-zone model have

been presented. Beckermann and coworkers [40] have presented a volume-averaged two-phase flow model to determine the velocities of both the solid and liquid phases at low fraction solid, and Nikrityuk et al [41] assumed rheological behavior over the entire mushy region. However, each of these formulations assumed laminar flow in both the bulk liquid and mushy regions. Recently, Pardeshi et al extended this the hybrid flow model to describe solidification in the presence of turbulent flow [42]. In this model, the k - ϵ model to describe the turbulent characteristics in the bulk liquid and at low fraction solid. However, the model does not account for flow damping via the interaction of the turbulent eddies and the solid crystallites. This interaction has been experimentally shown to have a key role in damping the flow intensity in the liquid phase, and must be considered in the analysis to accurately predict the liquid velocity, and due to the strong coupling between the flow and other transport variables, the extent of solute segregation and the temperature gradient.

Previous work by the author [43] led to the development of a rudimentary formulation for describing the flow damping by the turbulent crystallite interactions in the mushy region. In this model, an equivalent damping point force was derived by assuming homogeneous turbulence, with the force being described in terms of the turbulent kinetic energy, the fraction solid, and the coherency fraction solid. Although the results were consistent with expectations, the model had several pitfalls, particularly with respect to the direction in which the point force was applied, which was assumed to be invariant.

The endeavor of this research will be on developing realistic modeling tools for describing the electromagnetic, temperature, concentration, and velocity fields in EM stirred processes during solidification. The goals may be succinctly stated as follows:

- (1) To develop a methodology for describing the contribution of turbulence in damping the flow in the mushy zone.
- (2) To develop a methodology that solves the electromagnetic field and the conservation equations for temperature, solute concentration, and fluid flow in solidification processes.
- (3) To investigate the effect of solidification parameters, namely the crystallite size and solidification morphology, on the flow behavior in the bulk and mushy zone during solidification.
- (4) To determine the model's capability to accurately predict the solute segregation patterns found by experiments.
- (5) To determine the effect of the flow characteristics on the extent and pattern of macrosegregation in the mushy region during solidification.
- (6) To determine the effects of induction coil design, namely the coil position and configuration, on the pattern and intensity of the flow in both the bulk liquid and the mushy region.

This dissertation will proceed as follows:

- Chapter two will provide a review of techniques used in literature for describing the electromagnetic, heat transfer, fluid flow, and solute segregation phenomena in EM stirred solidification systems.
- Chapter three will present a manuscript published in *Metallurgical and Materials Transactions B* [44] which describes the basic formulation used in this study along with preliminary results.

- Chapter four will present a manuscript published in *ISIJ International* [45] that employs this model presented in Chapter 3 in discussing the influence of key coil design parameters on the solidification behavior.
- Chapter five will present a manuscript submitted to the *International Journal of Cast Metals Research* that will expand the model presented in Chapter three to determine the effects of the turbulent damping model to solute segregation and compare the computed results with experimental measurements.
- Chapter six will briefly review the principal findings of these research studies, along with several suggestions for future research topics which may be further explored at a later date.

Chapter 2

Literature Review

There has been significant progress made in simulation techniques for describing the electromagnetic, fluid flow, heat transfer, and mass transfer phenomena in solidification processes. This chapter will provide an overview of previously published literature on numerical simulation of the electromagnetic, temperature, solute, and velocity fields in solidification systems.

2.1—Computational Electromagnetics

The electromagnetic field quantities are governed by the Maxwell equations. Namely, these are the differential formulations of the integral Gauss laws for conservation of the electric and magnetic fields, Ampere's law for describing the relationship between the electric current and the magnetic field, and Faraday's law of induction. The flow characteristics in EM stirred systems strongly depend on the type of field used. The most commonly used are stationary [3, 22], rotating [34, 41, 42], and traveling magnetic fields [22, 30].

Although the discussion of literature will be focused primarily on solving the electromagnetic field numerically, it is necessary to note for the purposes of rigor that a majority of models for EM solidification systems have employed approximate analytical solutions [38, 42, 46-48] for describing the resulting Lorentz force field in the melt. While such solutions are simple to implement and saves computing time for solving the EM field in the molten metal, they suffer from several drawbacks. First, these solutions may only be obtained for highly simplified infinite or semi-infinite systems possessing a significant degree of symmetry, making them untenable for more complex, finite geometries. This is especially made clear for rotary

stirring, where Davidson and Boysan [49] examined the flow in rotary stirring of round billet castings. They found that the flow induced in the round is a superposition of the primary, rotational flow resulting from the applied rotating field and a secondary, axial flow driven by the gradient of the EM force near the top and bottom boundaries of the stirrer. This is made even clearer by the work of Schwerdtfeger and colleagues [48] on modeling idealized continuous casting systems. By simplifying the EM field problem to two dimensions, only the primary flow field in the molten pool was resolved. The secondary flow field predicted by Davidson and Boysan [49] was later confirmed by Meyer et al [3], who solved the EM field problem numerically for finite sized continuous casting systems.

Secondly, the assumptions made for approximate analytical solutions made them ill-suited to accommodate the presence of adjacent conducting materials, which act as magnetic shields and distort the magnetic flux lines around the induction coil. This leads to variations of the Lorentz force within the molten metal, changing the flow pattern. An example of this may be found in the work of Vives and Ricou [50], who examined the effect of placing copper magnetic shields on the flow structure in a coreless induction furnace.

This articulates the need for a numerical solution to the EM field problem. Most computational techniques for numerically computing the EM field quantities are based on solving the differential forms of the Maxwell equations based on potential formulations for the electric field, \mathbf{E} , and the magnetic field, \mathbf{B} . Use of potentials allows for simplified handling of the boundary conditions and discontinuities in the tangential component of the electric field and the normal component of the magnetic field. Potentials may be generally classified into two types: (i) scalar potentials and (ii) vector potentials. The most frequently used scalar potentials in formulations alternating EM field problems are the electric scalar potential, V , and the reduced

magnetic scalar potential, ψ . Similarly, the most common vector potentials are the magnetic vector potential, \mathbf{A} , and the current vector potential, \mathbf{T} . The differential equations using scalar potentials are of Laplace-Poisson type, while the governing vector potential equations are diffusion-type for eddy current problems.

Most formulations for eddy current problems have been primarily based on the magnetic vector potential. Roger and Eastham [51] used the vector potential \mathbf{A} for the field conductor, along with scalar potentials, namely ψ for free space and ϕ for ferromagnetic materials, in the non-conducting media. The Biot-Savart law was used to describe the source fields (i.e. from the coil). While this does allow for a solution to be obtained, this method suffers from two principal drawbacks. First, this method only works for singly-connected conducting domains, meaning that it cannot accommodate the presence of magnetic shields. Furthermore, the method requires that the domain have uniform electrical conductivity, which is not physically valid during solidification.

The remedy to the latter problem was put forth by Pillsbury [52], who introduced the $\mathbf{A}, \mathbf{V}-\phi$ formulation to allow for variable electrical conductivity. In that work, the magnetic and electric fields by solving for \mathbf{A} and \mathbf{V} , respectively, with ϕ being used to determine the field in free space. However, the use of the magnetic scalar potential in free space means that this method still does not allow for magnetic shields. To remedy the magnetic shield drawback, Roger et al [53] proposed a form of domain decomposition by using cuts in the conductor in the direction of the current. However, implementation of this proposal requires special routines to deal with discontinuities at the domain boundaries, increasing the computational complexity of the problem. The multiply-connected domain problem was remedied by both Chari et al [54] and Biddlecombe et al [55], who both introduced the $\mathbf{A}, \mathbf{V}-\mathbf{A}$ formulation. This allows for the

presence of multiple conductors in the overall solution domain without the need for stiff current sources—the assumption that the induced currents do not influence the source current—at the cost of increased degrees of freedom.

The use of the current vector potential appeared in the literature more recently, with Carpenter et al [56-58] first suggesting such a formulation. Preston et al [59] was the first to use the \mathbf{T} - ψ , ψ formulation. Here the current vector potential was used to solve the eddy current distribution within the conductor, and the magnetic field was represented by the reduced scalar potential. To enforce continuity of the current vector potential at the boundaries, a gauge condition was used, meaning that the formulation can be applied to problems involving multiply-connected domains. The computational advantages associated with various magnetic and current vector potential formulations were investigated by Reinhart [60] and Biro [61].

Solutions of the differential equations are generally carried out using the finite element method, finite difference method, or the control volume techniques. For further details, the reader may refer to References [62-64]. The principal drawback with these solution methods is that eddy current problems are open bounded in nature, meaning that the solution domain must not only include the conducting regions, but free space as well in order to properly define the boundary conditions of the solution domain, causing significant computational inefficiency.

This drawback may be remedied through the use of hybrid techniques. These techniques employ two different solution methods in such a way that the weakness of one solution method is compensated by the strength of the counterpart method. In the hybrid boundary element/FEM technique of Salon [65], the differential vector potential equation is solved using the finite element method, while the boundary element method is used to resolve the boundary conditions. El-Kaddah and coworkers [66] used the control volume/integral method. In this procedure, the

control volume technique is used to solve the magnetic diffusion equation for \mathbf{A} within the conductor, while the boundary conditions are resolved using the Biot-Savart law. An analogous procedure was developed using the finite element method by El-Kaddah and Natarajan [67, 68]. These hybrid methods were later shown to be more computationally efficient than any of the various standalone methods [69].

In two dimensional systems or three dimensional ones possessing a symmetry plane, it is advantageous to solve the EM field problem using the integral formulation. The most renowned of these formulations is the mutual inductance method first introduced by Kolbe and Reiss [70] and applied to induction heating problems by Dudley and Burke [71]. In this method, the system is divided into a elementary circuits whose volume elements possess constant current density. The eddy currents in each circuit may be expressed in terms of the contributions of all other circuits in the system, and the resulting set of simultaneous equations are solved to yield the current distribution. Relations for calculating the self-inductance and mutual inductance may be easily found in electrical engineering textbooks [72]. Complementing this method's simplicity is the fact that it may be used to solve the EM field problem in multiply-connected arbitrary domains without having to grid free space. This method has been applied to modeling material processing systems such as induction furnaces [21, 25, 26, 30, 73], the continuous casting of aluminum [3, 74], and levitation melting systems [75].

2.2—Modeling of Heat Transfer during Solidification

Solidification is a classical moving boundary problem which involves the transfer of heat and mass. Development of mathematical modeling tools to describe solidification processes

involving the solution of the heat, mass and momentum transfer equations is of paramount importance in order to understand and predict solidification phenomena.

Initial efforts to develop a mathematical description of solidification processes were focused on idealized problems assuming no convection in the liquid phases (i.e. stagnant liquid) and pure materials. Such studies were later expanded to include alloy systems.

2.2.1—Isothermal Solidification

Solidification of pure metals or other materials which undergo isothermal phase change (e.g. eutectic alloys), constitute a well-known class of moving boundary problems known as Stefan problems. The solution of these problems requires determining the temperature profile in each phase via the solution of the heat conservation equations for both the solid and liquid, respectively, followed by foreknowledge of the rate of solidification front advancement in order to resolve the Stefan conditions at the interface.

The earliest solutions of one dimensional Stefan problems were exact analytical in nature for a semi-infinite medium by employing a similarity solution technique, transforming the partial differential equations into ordinary ones. Such an approach is necessary due to the non-linear nature of the energy balance at the interface. Those interested in the mechanics of these solutions may refer to the heat transfer text of Eckert and Drake [76]. In order to obtain such solutions, however, numerous assumptions and simplifications are required; this limits their applicability with regards to bounded systems. To this, approximate integral methods were developed for specific bounded systems by Goodman [77], Lightfoot [78], Rathjen and Jiji [79], and Budhia and Krieth [80]. However, these methods still require a number of simplifications, and thus will

not be discussed further in the context of this work. For more information on solution of Stefan problems, see the text of Rubenstein [81].

The limitations of the previously mentioned analytical methods led to the development of numerical solutions of Stefan problems in multiple space coordinates. Since isothermal phase change materials feature a sharp, distinct interface, there is a likewise strong discontinuity. This discontinuity may be treated with the use of front-tracking, boundary immobilization, or specific heat methods.

Murray and Landis [82] were the first to introduce the front-tracking approach. In this solution method, the grid features a set of zero dimensional marker nodes to explicitly define the interface location, and are connected using a piecewise function—typically a polynomial. While the grids located at a distance from the moving boundary are fixed and regular in shape, those nearest the interface are deformed and irregular in shape. In the work of Unverdi and Tryggvason [83], an indicator function was used to define the interface by assigning integer values to each phase. The marker nodes were then defined using an interpolant based off the interfacial energy balance, and the nodes were allowed to propagate through the fixed grid. However, this method cannot easily handle three dimensional solidification. This led to the level set method of Osher and Sethian [84], which relies on the determination of a level set function that satisfies the Hamilton-Jacobi equation. The interface is defined as the zero level set. Implementation is computationally expensive, however, due to the method requiring a very fine grid structure near the interface.

Boundary immobilization methods solve the governing heat equation by transforming each single phase domain from real space to a non-orthogonal computational space. The interface in this new system lies on a single, fixed coordinate surface with mobile outer

boundaries, making the solution method Lagrangian in form. This method was first employed for one dimensional interfaces by Crank [85] and later extended to two dimensions by Duda et al [86] for phase change of a finite bounded cylinder. In Saitoh [87], the system was mapped using the Landau transformation, which reduces the number of space variables by one. Each of the previous studies used the finite difference method to achieve a solution, while Hsu et al [88] used the control volume method to solve the transformed equations. Although boundary immobilization has been shown to produce accurate solutions to benchmark problems, the transformed equations contain nonlinear cross-derivative terms consisting of multiple spatial derivatives, making implementation cumbersome.

The specific heat method, first introduced by Thionov and Samarskii [89], avoids the need to explicitly discretize the boundary by introducing an effective specific heat capacity in the neighborhood of the transformation temperature by assuming that the discontinuity in enthalpy can be represented by an extremely narrow freezing range. This allows the latent heat term in the heat conservation equation to be rewritten in terms of a piecewise specific heat function. A thorough introduction of the method may be found in Szekely and Themelis [90]. The first applications of the specific heat method is found in Soviet literature [91, 92]. For materials which undergo isothermal phase change, the specific heat function for latent heat release was assumed to be linear with temperature.

2.2.2—Solidification of Alloys

Unlike pure materials, most alloys do not undergo isothermal phase change; instead, the transition from the liquid to solid phase occurs over a temperature range. Alloy solidification begins at liquidus temperature, and concludes at the solidus temperature. Due to the incremental

nature of the phase change, front tracking and boundary immobilization algorithms are not applicable to modeling alloy solidification at the macroscale.

Latent heat evolution during alloy solidification is determined by the transformation kinetics. Models representing this evolution may be divided into two categories, namely empirical and deterministic formulations. In empirical models, the fraction solid is given as a continuous function of temperature. There are a number of functions available to represent the fraction solid. The simplest is that where the fraction solid is given as a linear function of temperature, as seen in the works of Voller and Prakash [32], Chang and Stefanescu [93] and Poole et al [6], among others. Other relations that have been used is the lever rule used by Incropera and colleagues [33, 38], and the Scheil relation used by Santos et al [94]. However, empirical models do not include any information regarding the microstructural features of the crystallites in the mushy region. First proposed by Oldfield [95], deterministic models determine the value of solid fraction via nucleation and growth laws rather than temperature dependent functions. The heat evolved is then given by the change in volume of the growing nuclei and crystallites. This approach was then applied by Stefanescu and colleagues [96, 97] for predicting the cooling curves of cast iron and by Budenkova et al [98] and Wu et al [99] for solidification of Al-Si alloys.

2.3—Modeling of Fluid Flow during Solidification

Early models for solidification assumed that the molten material was quiescent, making the convective derivatives zero, for the sake of simplifying the solidification problem.

Experimental observations, however, have shown that this assumption is quite rare, and the presence of fluid flow and convective heat and mass transfer leads to significant deviation from

diffusion-only solutions. Such phenomena have been shown to have a strong influence on microstructural development and segregation profiles of the final cast product [10-21].

There are two fundamental regimes of convective transport during solidification: (i) natural convection and forced convection. In natural convection, also referred to as thermosolutal convection, fluid flow occurs as a result of thermal and solute gradients in the liquid phase. The relative intensity of natural convection in the system is defined by the Rayleigh number, which is the ratio between the buoyancy and viscous forces. Theoretical studies [100, 101] found that the critical value of the Rayleigh number for the onset of natural convection in alloys to be $\sim 10^4$.

Experiments involving aqueous alloys have shown that fluid flow causes alterations in the solidification velocity and curvature of the melt front [102, 103], which are both important in determining the solidification morphology and grain size [104]. Furthermore, macrosegregation is directly caused by transport of rejected solute via interdendritic and bulk flow throughout the solidifying cast alloy [105].

Forced convection, however, occurs via applied body forces originating from an external source. These forces may be based on mechanical [106], ultrasonic [107], or electromagnetic phenomena. The effects of forced convection on the micro- and macrostructure have been well-documented. Liu et al [12] found that forced convection homogenized the alloying elements in the AZ91 melt, and also improved solution strengthening of the alloy. Kuznetsov [108] found considerable inverse macrosegregation of carbon in twin-rolled cast steels. However, the most important role of stirring is that of grain refinement via the dendrite fragmentation mechanism, as this increases the nucleation potential of the melt [19-21].

While much focus has been dedicated to understanding the flow in the bulk liquid in metalcasting systems, convection, regardless of source, is also found in the mushy region as well

[109, 110]. There have been several formulations proposed in order to understand the flow in these two domains. Such formulations may be succinctly characterized as either (i) single-zone or (ii) dual zone models.

2.3.1—Single Zone Models

In single-zone formulations, the dendrites are assumed fixed in place for all values of fraction solid greater than zero, and thus may be treated as a porous medium that obeys Darcy's law. The permeability decreases with increasing fraction solid, leading to increased damping of the flow as solidification progresses. The first model was that introduced by Mehrabian et al [111] to describe the role of interdendritic flow on solute redistribution, but the solution domain was restricted to the mushy region only. Szekely and Jassal [112] later expanded the model to include the contributions of the bulk liquid flow on solute redistribution.

The permeability relations are expressed in terms of the geometry of the crystallites in the porous medium and their respective instantaneous grain size. The geometrical dependence of the permeability means that there may exist a high degree of anisotropy depending on the directionality of the flow, making the permeability a tensor of second order. However, for macroscale modeling of equiaxed solidification, the orientations of the crystallites in the control volume are assumed to be random, leading to the geometrical dependence of the permeability to be taken as isotropic. A number of permeability models have been used in modeling solidification systems. The Hagen-Poiseuille model describes the permeability assuming laminar flow through a bundle of tubes [31, 36, 111]. This is a good approximation for columnar solidification, and was primarily used in studies by Mehrabian and coworkers [31, 111]. In the case of equiaxed and globular morphologies, the permeability is given by the Kozeny equation

and its derivatives [35, 113], which assume laminar flow through an array of packed spheres. Use of the Kozeny relationships may be found in Voller and Prakash [32], Incropera [33, 38], and Campanella [34] among others. It should be noted that other analyses have been performed to adjust the permeability relations to account for the tortuosity of dendritic morphological structures [114].

It should be noted that the assumptions used for single-zone models, particularly the permeability relations, are valid for laminar flow only; however, there have been attempts to account for turbulence in the mushy region. Shyy et al [37, 115] was the first to incorporate turbulence in single-zone models. The model accounted for damping of turbulence using a low Reynolds number k - ϵ model. However, the Shyy formulation only assigned an ad-hoc functional dependence to the turbulence constant C_{μ} , leaving the constants associated with turbulent generation unaltered and thus preventing closure of the k and ϵ equations. Prescott and Incropera [38] represented the first attempt to describe turbulent flow in EM solidification systems. The model used the low-Re k - ϵ of Jones and Launder [116]. Although turbulent closure was attained and reported significant damping of turbulence in the mushy region, the formulation incorporated Darcy-like terms into the k and ϵ equations. Such relations do not reflect the physics of the problem for two reasons, as (i) Darcy's law only applies to laminar flow and (ii) the turbulent mixing length within the interdendritic region quickly become on the order of the Kolmogorov length scale, making the flow essentially laminar with regards to macroscale flows [117].

2.3.1—Dual-Zone Models

Although single-zone models have proven useful in describing interdendritic flow for castings exhibiting columnar grain structures, experimental investigations [109, 110] have found the porous medium assumption to be wholly inadequate for equiaxed solidification, where the crystallites travel with the liquid and form a slurry. It was also found that Darcy behavior only occurs at higher solid fraction [109, 110].

This presents the impetus for a new model to account for the varying behavior of the crystallites with respect to fraction solid. The first attempt was made by West [118], which used a piecewise function for the permeability function. This was used by Amberg [119] for macrosegregation of steel. Although this addresses the dualistic behavior of equiaxed crystallites in the mushy region, the model still does not account for the dynamic behavior of the crystallites at low fraction solid. Furthermore, for reasons previously mentioned, the West model may not be applied to turbulent flow regimes.

Oldenburg and Spera [39] accounted for the traveling crystallites by relaxing the packed bed assumption at low fraction solid and splitting the mushy region into two flow domains, shown in Figure 2-1. In the suspended particle region, the liquid and crystallites were treated in aggregate as a slurry. The flow in this region was treated as that of a “pseudofluid” using the homogeneous flow model, with the viscosity having dilatant behavior. The porous medium relation was retained for the fixed particle region. The two domains were separated using the coherency fraction solid, whereby the crystallites begin to come into contact with one another and form an interlocking mesh. This approach was applied by Chang and Stefanescu [93] and Mat and Ilegbusi [120] in modeling shrinkage-driven macrosegregation in metal alloys and aqueous analogues.

While the Oldenburg and Spera formulation accurately reflects the physical phenomena associated with equiaxed solidification, the original formulation is limited to laminar flow; however, forced convective flows are typically highly turbulent [3, 21, 50]. Pardeshi et al [42] recently presented a dual-zone formulation that accounts for turbulent behavior by using the high-Re k - ϵ model of Launder and Spalding [121] throughout the bulk liquid and the mushy region. However, use of this model in the fixed particle region leads to the same mixing length pitfalls as was found for Prescott [38] and Shyy [37,115], making closure unattainable.

However, the greatest drawback of the Pardeshi model lies in the lack of accounting for momentum damping in the suspended particle region. It was shown as early as Brinkman [122] that there is an additional friction force exerted by the solid phase in the turbulent particle flows, with a similar results being found by Saffman [123] and Sproull [124]. In his study on ice slurry flows, Shire et al [125] noted that the phenomenon of “re-laminarization” was more prominent at higher values of ice fraction, and theorized that it was due to the slurry preventing the generation of turbulence. Yamagishi et al [126] further elaborated on re-laminarization, attributing it to the turbulent mixing length becoming on the same order as the particle size. For further instances of laminarization in initially turbulent slurry flows, the reader is also referred to the studies of Wenji et al [127] and Alvarado et al [128]. It should be noted that Budenkova et al [98] made attempts to account for the interactions between the crystallites and the turbulent eddies using a damping function. While turbulence was damped, the expressions used were ad-hoc in form and lacked any physical foundation.

2.4—Modeling of Solute Segregation during Solidification

The redistribution of solute at the solid-liquid interface induces spatial variations in the concentration of alloying elements within the casting, commonly referred to as segregation. Such variations are deleterious to ensuring uniform physical properties within the cast alloy, and thus should be minimized. Solute segregation phenomena may be divided into microsegregation and macrosegregation. Microsegregation takes place at the interface due to differences between the solute solubility in the different phases, while macrosegregation takes place due to the bulk transport of solute enriched (or depleted) liquid throughout the casting. It should be noted that macrosegregation is present even in the absence of stirring forces.

Since the focus of this work is macroscale modeling, only macrosegregation will be discussed. The first macrosegregation models were developed by Kirkaldy and Youdelis [129], Flemings and Nereo [130], and Mehrabian et al [111]. These models were applied to shrinkage-driven and buoyancy-driven flows, and are able to predict the occurrence of inverse segregation in cast Al-Cu alloys. However, these models are applicable to flow in the mushy region only and cannot be used for forced convective flows.

The first model to include the effects of bulk liquid flow on macrosegregation was that of Ridder et al [31]. In this formulation, the solidifying domain was divided into the mushy and bulk liquid regions (i.e. single-zone model). The shrinkage-induced flow field was calculated from Darcy's law. The flow in the bulk liquid was determined via stream function solutions, and the two flow fields were resolved using pressure-based boundary conditions applied at the liquidus isotherm. The solute field was then calculated using the local solute redistribution equation of Flemings and Nereo [130]. Although the Ridder model does accurately predict segregation profiles found in Pb-Sn castings; however, the domain decomposition method

employed can only be used for steady state problems, as the conforming mesh used to obtain a solution relies on the foreknowledge of the liquidus isotherm position.

The development of continuum models in the eighties allowed for the description of solute transport in both the bulk liquid and mushy regions. First introduced by Bennon and Incropera [33] and Voller and Prakash [32], such models using mixture theory in defining the solute concentration within a given control volume, whereby the conservation equations in each phase are summed with respect to the relative presence of each phase within the control volume. The thermophysical properties (e.g. mass diffusivity) of the mixture are similarly treated. Such approaches allow for a simplified solution of the resulting equations for fixed grids without explicitly having to define interface locations.

The coupling of the micro-scale segregation phenomena with continuum formulations is necessary to determine the rate of solute rejection into the surrounding liquid. The simplest method of coupling is through assuming the diffusional behavior of solute in each phase. Early continuum models such as that of Bennon and Incropera [33] assumed complete diffusion within each phase and, by corollary, compositional homogeneity within each phase. The lever rule, as it is often referred, has been applied in a clear majority of macrosegregation studies, examples of which may be found in References [33, 42, 131, 132]. However, the assumption of significant solid state diffusion is not physically valid, as the value of mass diffusivity in the solid to be several orders of magnitude smaller than that of the liquid.

Recognizing this, Rappaz and Voller [133] proposed an alternative approach by assuming no diffusion within the solid phase while maintaining complete diffusion in the liquid (aka Schiel assumption). This allows for the elimination of solid diffusion terms within the overall conservation equation and, by assuming equilibrium conditions at the solid-liquid interface,

allows for the determination of the overall solute balance while only solving for the liquid concentration only. This method was applied in the study of inverse segregation of Al-Cu alloy by Chang and Stefanescu [93] using a dual-zone flow model, and was found to be in good agreement with measurements; the model was also employed by Barman and Dutta [47]. There have also been efforts to incorporate a finite amount of solid state diffusion into the solidification model, as reflected later formulations by Voller and colleagues [134-136]. However, as noted in the vanguard work [133], the principal drawback of this model lies in its use of the interfacial equilibrium assumption. While it may be used for solidification problems, it may not be applied in reverse; that is, the assumption is invalid for remelting problems unless the freezing history is known.

Chapter 3

An Improved Model for the Flow in an Electromagnetically Stirred Melt during Solidification

3.1—Abstract

A mathematical model for simulating the electromagnetic field and the evolution of the temperature and velocity fields during solidification of a molten metal subjected to a time-varying magnetic field is described. The model is based on the dual suspended particle and fixed particle region representation of the mushy zone. The key feature of the model is that it accounts for turbulent interactions with the solidified crystallites in the suspended particle region. An expression is presented for describing the turbulent damping force in terms of the turbulent kinetic energy, solid fraction, and final grain size. Calculations were performed for solidification of an electromagnetically stirred melt in a bottom chill mold. It was found that the damping force plays an important role in attenuating the intensity of both the flow and turbulent fields at the beginning of solidification, and strongly depends on the final grain size. It was also found that turbulence drops significantly near the solidification front, and the flow becomes laminarized for solid fraction around 0.3.

3.2—Introduction

Electromagnetic (EM) stirring has found extensive use in solidification processing as a means to produce a fine, equiaxed grain structure [1-3]. The role of the flow is to homogenize the solute and temperature profiles in the bulk liquid [4,5], which affects segregation in the cast product. It also increases the nucleation potential in the melt through a combination of dendrite fragmentation [6-8], a decrease of the temperature gradient at the solidification front [9], and an

increase the dissipation rate of the melt superheat [10]. Clearly, an improved understanding of the flow characteristics in the bulk and mushy zones during solidification is critical in order to control the structure of the final product.

There are essentially two basic approaches for modeling the flow in the mushy zone, namely single-zone [11] and dual-zone models [12]. The single-zone model treats the entire two-phase region as a porous medium, with the flow being damped via Darcy's law. Although this model provides an adequate representation of the flow in columnar solidification, it is not suitable for equiaxed solidification, as the crystallites have been shown to travel with the flow prior to coalescence [13]. The dual-zone model addresses this problem by dividing the mushy zone into two domains: (i) the suspended particle region, and (ii) the fixed particle region, with the transition between regions occurring at the coherency point.

Recently, efforts have been made to model EM solidification processes [14-21]. With no exception, all models used an approximate analytical solution for describing the EM force field in the bulk liquid and two phase regions. In modeling the flow in the mushy zone, all of these studies, except for the works of Pardeshi et al [20] and Budenkova et al [21], employed a single-zone model for describing fluid flow in the mushy region. Several approaches have been used to model the turbulent field in the two phase region. Prescott and Incropera [15,16] and Shyy et al [17,18] determined the turbulent field using a low-Re $k-\epsilon$ model, together with ad-hoc expressions for the decay of the turbulent viscosity in the two phase region. Pardeshi et al [20] and Budenkova et al [21] employed high-Re $k-\epsilon$ model to describe the turbulent characteristics in the bulk liquid and suspended particle regions. Their formulation does not account for the damping of turbulence in both the suspended and fixed particle regions. Furthermore, the

interaction between the turbulent eddies and the solid crystallites, which is known to produce an additional damping force on the flow field [22-24], was not addressed in these models.

This paper presents a comprehensive model for the numerical calculation of the electromagnetic, velocity and temperature fields in an axisymmetrical EM stirred melt during solidification. This model uses a dual-zone approach for the flow in the mushy zone, and accounts for the damping of turbulence using the low-Re $k-\epsilon$ model, along with a turbulent damping force resulting from the interactions between the turbulent eddies and the crystallites in the suspended particle region. The model is then demonstrated for unidirectional solidification in a bottom-chill mold stirred using an induction coil.

3.3—Model Formulation

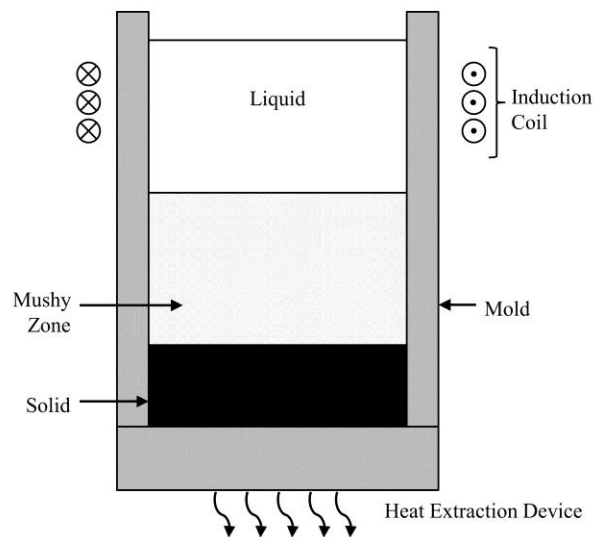


Figure 3.1—Sketch of a typical EM stirred solidification system

Figure 3.1 shows a typical EM stirred solidification system. As seen in this figure, the system is comprised of a container and heat extraction devices, surrounded by induction coil. An electric current is passed through the coil to induce eddy currents in the metal. The induced

currents generate both heat via electrical energy dissipation and Lorentz forces, which drive the flow in the bulk liquid and mushy zones. Numerical simulation of the solidification process must involve calculation of the EM field in the metal and other conducting domains, the velocity and turbulent fields, and the temperature field.

3.3.1—Electromagnetic Field

In this work, the electromagnetic field was calculated by solving the integral form of the Maxwell equations using the mutual inductance method [25-28]. In this method, the system (the metal and the magnetic shields) are divided into a number of elementary circuits, each of which is considered to be a region of constant current density, \mathbf{J} . For a time-harmonic two dimensional field, the induced currents in the elementary circuits can be represented by the following set of algebraic equations:

$$\oint \mathbf{J} \cdot d\mathbf{l}_i = -j\omega\sigma \left[\sum_{m=1}^{metal} M_{i,m} (\mathbf{J} \cdot \mathbf{S})_m + \sum_{c=1}^{shields} M_{i,c} (\mathbf{J} \cdot \mathbf{S})_c + \sum_{k=1}^{coil} M_{i,k} I_k \right] \quad [3-1]$$

where j is the square root of -1, σ is the electrical conductivity, μ_0 is the magnetic permeability of free space, $d\mathbf{l}$ is the length of the circuit, \mathbf{S} is the cross-sectional area of the circuit, and $M_{i,k}$ is the mutual inductance given by

$$M_{i,k} = \frac{\mu_0}{4\pi} \iint \frac{d\mathbf{l}_k \cdot d\mathbf{l}_i}{r'} \quad [3-2]$$

From the induced current, the magnetic flux density, \mathbf{B} , can be obtained from:

$$\mathbf{B} = -\frac{\nabla \times \mathbf{J}}{j\omega\sigma} \quad [3-3]$$

Finally, from the induced current and magnetic fields, the electrical energy dissipation (Joule heating), S_{em} , and the Lorentz force distribution in the melt, \mathbf{F}_{em} , can readily be calculated from

$$S_{em} = \frac{1}{2} \operatorname{Re} \left(\frac{\mathbf{J} \cdot \mathbf{J}^*}{\sigma} \right) \quad [3-4]$$

$$\mathbf{F}_{em} = \frac{1}{2} \operatorname{Re} (\mathbf{J}^* \times \mathbf{B}) \quad [3-5]$$

where \mathbf{J}^* denotes the complex conjugate of the current density.

3.3.2—Heat Transfer

The general energy equation that describes heat transfer and solidification in the metal domain is

$$\rho c_p \left(\frac{\partial T}{\partial t} + \mathbf{u} \cdot \nabla T \right) = \nabla \cdot (k^* \nabla T) + S_{em} + \rho L \frac{df_s}{dt} \quad [3-6]$$

where ρ and L are the density and latent heat of fusion, respectively. Assuming that solid fraction is a piecewise linear function of temperature, the latent heat term in Eq. (3-6) may be eliminated and the specific heat, c_p , may be replaced by an effective specific heat C^* , where

$$C^* = \begin{cases} c_{p,l} & T \geq T_L \\ c_{p,s} + L \sum_{i=1}^n \frac{1}{T_i - T_{i+1}} & T_S < T < T_L \\ c_{p,s} & T \leq T_S \end{cases} \quad [3-7]$$

where n corresponds to the number of segments and T_i and T_{i+1} represent the temperatures defining an individual line segment in the solid fraction versus temperature curve. T_L and T_S are the liquidus and solidus temperatures, respectively, and the l and s subscripts correspond to the values for the respective liquid or solid phases. For convective heat transfer in turbulent flows, the effective thermal conductivity, k^* , is given by

$$k^* = \begin{cases} k_l + \frac{\mu_t c_{p,l}}{P_T} & T \geq T_L \\ (1 - f_s)k_l + f_s k_s & T_S \leq T < T_L \\ k_s & T \leq T_S \end{cases} \quad [3-8]$$

where μ_t is the turbulent viscosity and P_T is the turbulent Prandtl number.

3.3.3—Fluid Flow

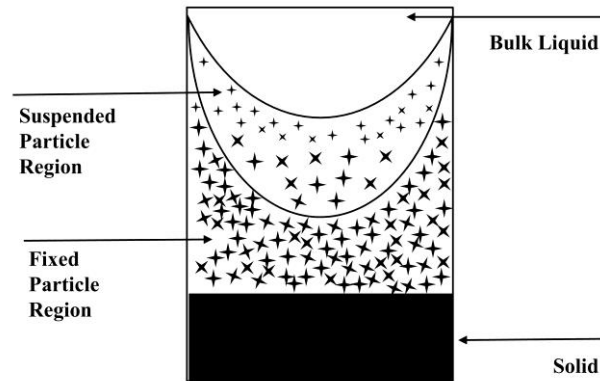


Figure 3.2—Flow domains for the dual-zone solidification model

Figure 3.2 shows the various flow domains in the dual-zone model, namely the bulk liquid, suspended particle region, and fixed particle region. In the suspended particle region, the flow is described using the homogeneous two-phase flow model, and the flow is driven by EM forces, as in the bulk liquid. In the present model, damping of the flow via interactions between the turbulent eddies and the solid crystallites is considered. In the fixed particle region, the flow is represented by Darcy's law. It should be mentioned that the Lorentz forces do not drive the flow in the interdendritic channels. In this work, the flow in the fixed particle region is assumed to be laminar, which is a reasonable assumption since the interparticle spacing is on the order of the Kolomogrov turbulent length scale [29].

The governing equations for incompressible flow are:

Continuity:

$$\nabla \cdot \mathbf{u} = 0 \quad [3-9]$$

where

$$\mathbf{u} = f_s \mathbf{u}_s + (1 - f_s) \mathbf{u}_t \quad [3-10]$$

Navier-Stokes Equation:

$$\rho \frac{\partial \mathbf{u}}{\partial t} + \rho \mathbf{u} \cdot \nabla \mathbf{u} = -\nabla P + \nabla \cdot \left(\mu (\nabla \mathbf{u} + \nabla \mathbf{u}^T) \right) + \lambda (\mathbf{F}_{em} + \mathbf{F}_d) - \frac{\mu^*}{K} (\mathbf{u} - \mathbf{u}_s) \quad [3-11]$$

where μ is the effective viscosity, and λ is a switch parameter, \mathbf{F}_d is the damping force due to turbulence interactions with the solid particles, and P is the pressure. For the suspended particle region, $\mathbf{u} = \mathbf{u}_s$, making the Darcy term equal to zero, and λ is equal to unity. For the fixed particle region, $\mathbf{u}_s = 0$ and $\lambda = 0$, and the permeability, K , is given by the Carman-Kozeny equation:

$$K = \frac{D_g^2 (1 - f_s)^3}{180 f_s^2} \quad [3-12]$$

where D_g is the final grain size.

The turbulent field is described using the low-Re k - ε model [30]. The conservation equations for k and ε are

$$\rho \frac{\partial k}{\partial t} + \rho \mathbf{u} \cdot \nabla k = \nabla \cdot \left(\frac{\mu_t}{P_k} \nabla k \right) + G_{ij} - \rho \varepsilon \quad [3-13]$$

$$\rho \frac{\partial \varepsilon}{\partial t} + \rho \mathbf{u} \cdot \nabla \varepsilon = \nabla \cdot \left(\frac{\mu_t}{P_\varepsilon} \nabla \varepsilon \right) + C_1^* G_{ij} \frac{\varepsilon}{k} - C_2^* \rho \frac{\varepsilon^2}{k} \quad [3-14]$$

where P_k and P_ε are the turbulent Prandtl numbers for k and ε equations, respectively, and μ_t is the turbulent viscosity given by

$$\mu_t = C_\mu^* \rho \frac{k^2}{\varepsilon} \quad [3-15]$$

In the low-Re k - ε model, the turbulence constants C_1^* , C_2^* , and C_μ^* are functions of the turbulent Reynolds number ($R_T = \rho k^2 / \mu_l \varepsilon$):

$$\begin{aligned} C_1^* &= C_1 \\ C_2^* &= C_2 \left(1 - 0.3 \exp(-R_T^2)\right) \\ C_\mu^* &= C_\mu \exp\left(\frac{-3.4}{(1 + 0.02 R_T)^2}\right) \end{aligned} \quad [3-16]$$

where μ_l is the laminar viscosity, and C_1 , C_2 , and C_μ are equal to 1.43, 1.92, and 0.09, respectively. The effective viscosity is the sum of the laminar and turbulent viscosity components. The laminar viscosity is determined from the rheological properties of suspensions [31], and for each flow domain may be expressed as:

$$\mu_t = \begin{cases} \mu_m & f_s = 0 \\ \mu_m \left(1 + 2.5 f_s + 10.05 f_s^2 - 0.0071 \exp(16.67 f_s)\right) & 0 < f_s < f_c \\ \mu_m & f_c \leq f_s \leq 1 \end{cases} \quad [3-17]$$

where μ_m is the molecular viscosity of the fluid.

3.3.4—Turbulent Damping Model

The damping force in the suspended particle region is

$$\mathbf{F}_d = (1 - f_L^2) \nabla \cdot \bar{\tau}_t \quad [3-18]$$

where f_L is the liquid fraction, and τ_t is the turbulent Reynolds stress. Detailed derivation of Eq. (3-18) is given in Appendix 3A. Following Bradshaw's turbulent model [32], the Reynolds stress can be written in terms of turbulent kinetic energy as:

$$\bar{\tau}_t = c_d^{1/2} \rho k \delta_{ij} \quad [3-19]$$

where c_d is a constant, and is equal to 0.08 [33]. Hence, the divergence of the Reynolds stress is:

$$\nabla \cdot \bar{\tau}_t = c_d^{1/2} \rho \nabla k \quad [3-20]$$

The grad term in Eq. (3-20) represents the change in turbulent kinetic energy between the surrounding liquid and the particle surface, where k is taken to be zero. For particles of instantaneous size d arranged in a cube of dimension D_g , the grad of the turbulent kinetic energy can be locally approximated by

$$\nabla k = \frac{2k}{(D_g - d)} \hat{\mathbf{e}}_j \quad [3-21]$$

From Eqs. (3-18), (3-20), and (3-21), the damping force is given by:

$$\mathbf{F}_d = (1 - f_L^2) \frac{2c_d^{1/2} \rho k}{D_g - d} \hat{\mathbf{e}}_j \quad [3-22]$$

where

$$d = D_g \left(\frac{6(1 - f_L)}{\pi\beta} \right)^{1/3} \quad [3-23]$$

The quantity β represents the particle-to-envelope volume ratio. The value of β for spherical particles is unity, and decreases with increasing sphericity. In addition, β also defines the coherency solid fraction ($f_c = \pi\beta/6$), which determines the boundary between the suspended particle and fixed particle flow domains. From Equations (3-22) and (3-23), the damping force can be written as:

$$\mathbf{F}_d = \frac{2(1 - f_L^2) \sqrt{c_d} \rho k}{D_g \left(1 - \left(\frac{6(1 - f_L)}{\pi\beta} \right)^{1/3} \right)} \hat{\mathbf{e}}_j \quad [3-24]$$

3.4—Solution Technique

The heat and fluid flow equations were solved using the control volume technique of Pun and Spalding [34]. In this technique, the solution domain was divided into a number of

contiguous volume elements. The momentum equations were discretized using the upwind scheme, and the resulting equations were solved iteratively. The pressure field was calculated using the SIMPLE algorithm of Patankar [35]. In these calculations, the solution was carried out for a 30 x 30 grid, which is sufficient to resolve the velocity and turbulent fields in EM induction stirring systems [27].

The magnetic field was calculated by dividing the metal and adjacent conducting regions into a number of elementary circuits. In order to accurately describe the decay of the magnetic field in the metal (skin effect), a finer grid was used near the outer radius of the conducting domains. The current density in each circuit is evaluated using Eq. (3-1), and the resulting set of simultaneous equations was solved using Choleski factorization. Upon obtaining the \mathbf{J} field, Ampere's law is used to obtain the \mathbf{B} field. From the computed \mathbf{J} and \mathbf{B} fields, the electromagnetic forces and Joule heating are calculated.

3.5—Results and Discussion

In this section, we shall present the computed results for unidirectional solidification of Al-4.5%Cu alloy in a bottom chill mold surrounded by an induction coil. The induction coil employed in this study consists of three turns situated in the middle of the crucible. The mold is comprised of an insulating refractory tube and a water-cooled stainless steel chill block. The dimensions of the system are given in Figure 3.3. Calculations were carried out for a coil current and frequency of 200 A and 500 Hz, respectively, a coherency solid fraction of 0.521, which corresponds to a globular solidification morphology, and the final grain size of the cast alloy, D_g , varying from 100 to 500 μm . The thermophysical properties used in this study are given in Table 3.1.

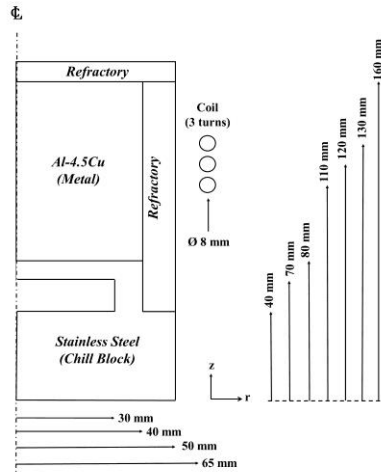


Figure 3.3—Dimensions of the system used in this study

| | |
|------------------------------|----------------------------|
| Solid density: | 2979 kg/m ³ |
| Liquid density: | 2979 kg/m ³ |
| Solid thermal conductivity: | 188.3 W/m-K |
| Liquid thermal conductivity: | 192.5 W/m-K |
| Solid heat capacity: | 870.5 J/kg-K |
| Liquid heat capacity: | 1059 J/kg-K |
| Electrical conductivity: | 1.28*10 ⁶ Mho/m |
| Liquidus temperature: | 921 K (648°C) |
| Solidus temperature: | 837 K (564°C) |
| Latent heat of fusion: | 389000 J/kg |
| Molecular viscosity: | 0.0015 Pa-s |
| Initial Temperature | 943K (670°C) |
| Heat Transfer Coefficient | 500 W/m ² -K |

Table 3.1—Thermophysical properties of Al-4.5%Cu alloy

Figure 3.4 shows the computed EM force field in the metal and the chill block. As seen in this figure, the EM force is at a maximum in the middle of the metal where the coil is located. It is also seen that the EM forces in the chill block are much smaller than those in the metal. Closer inspection of this figure shows that the EM forces near the chill block are higher than those at the top of the melt. This suggests that the vorticity of the EM forces, which drives the flow, will be asymmetrical, as shown in Figure 3.5. This figure also shows two counter-rotating vortices,

which suggests of two recirculating flow loops typical for a stationary magnetic field. The difference in the spatial variation of the vorticity, however, suggests that the intensity of the flow in each loop will be different. The distortion of the force field by the chill block underscores the necessity of including numerical computation of the electromagnetic field for simulating EM stirring processes.

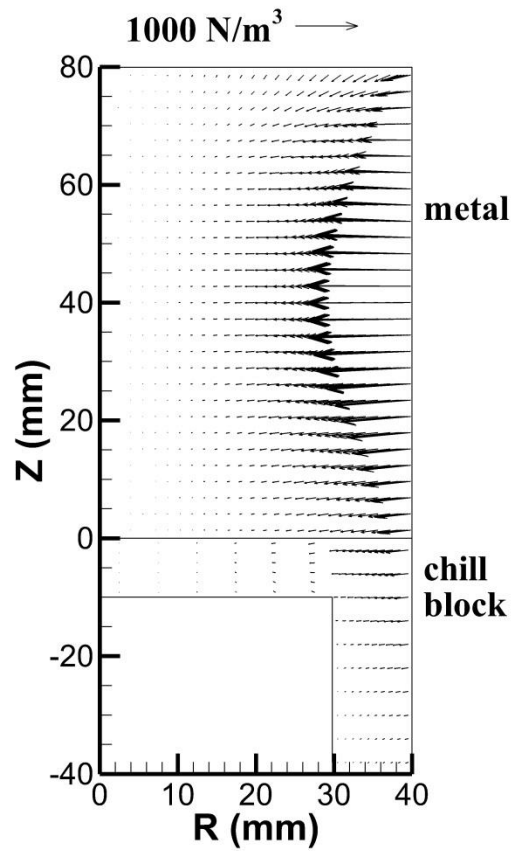


Figure 3.4—Computed Lorentz (EM) force field in the metal and chill block

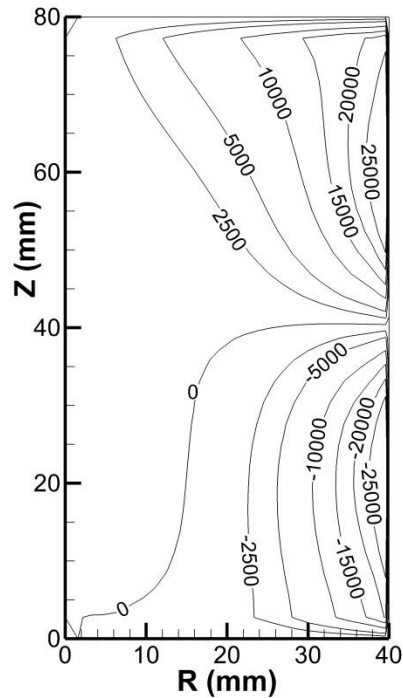


Figure 3.5—Computed vorticity of the EM force field in the metal

Figure 3.6 shows the initial velocity and turbulent fields of the flow prior to solidification. The turbulent field is represented in terms of the ratio of the turbulent to laminar viscosities, μ^* . As seen in Figure 3.6(a), the flow consists of two axisymmetric recirculating loops, consistent with the computed curl of the EM force field, Figure 3.5. For the given coil current and frequency, the characteristic velocity is around 25 mm/s. Closer inspection of this figure shows that the flow intensity in the upper loop is stronger than the lower loop. The maximum velocity in the upper loop is about 32 mm/s, while it is around 27 mm/s in the lower loop. Figure 3.6(b) shows that the turbulent viscosity is quite high, around 50 times the laminar viscosity of the liquid. It also shows that there is a significant spatial variation in the values of the turbulent viscosity, with the largest values found at the center of the vortices and at the free surface, where the shear strain rates are highest.

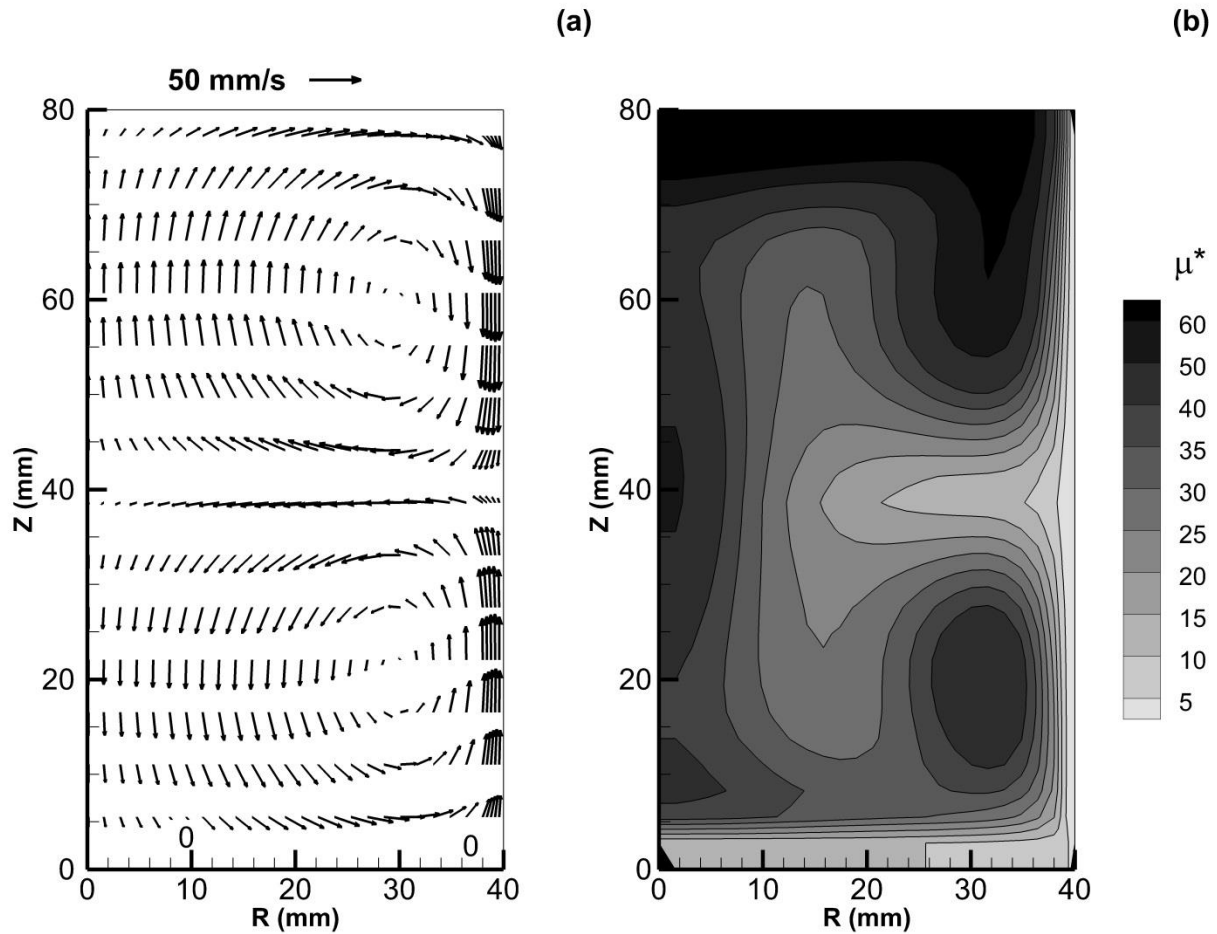


Figure 3.6—Initial characteristics of the flow: (a) velocity and (b) turbulent-to-laminar viscosity ratio

Figures 3.7(a) through 3.7(d) show the evolution of the velocity field during solidification at times of 30, 60, 120, and 240s, respectively. These results correspond to a final grain size of $500 \mu\text{m}$. When solid fraction is less than 0.05, Figure 3.7(a), the velocity field is essentially the same as that prior to solidification and the characteristic velocity is around 22 mm/s . After 60s, Figure 7(b), there is some reduction in the flow intensity. This is particularly more noticeable in the lower loop, where solid fraction is around 0.15. The characteristic velocity of the flow in this region is about 15 mm/s .

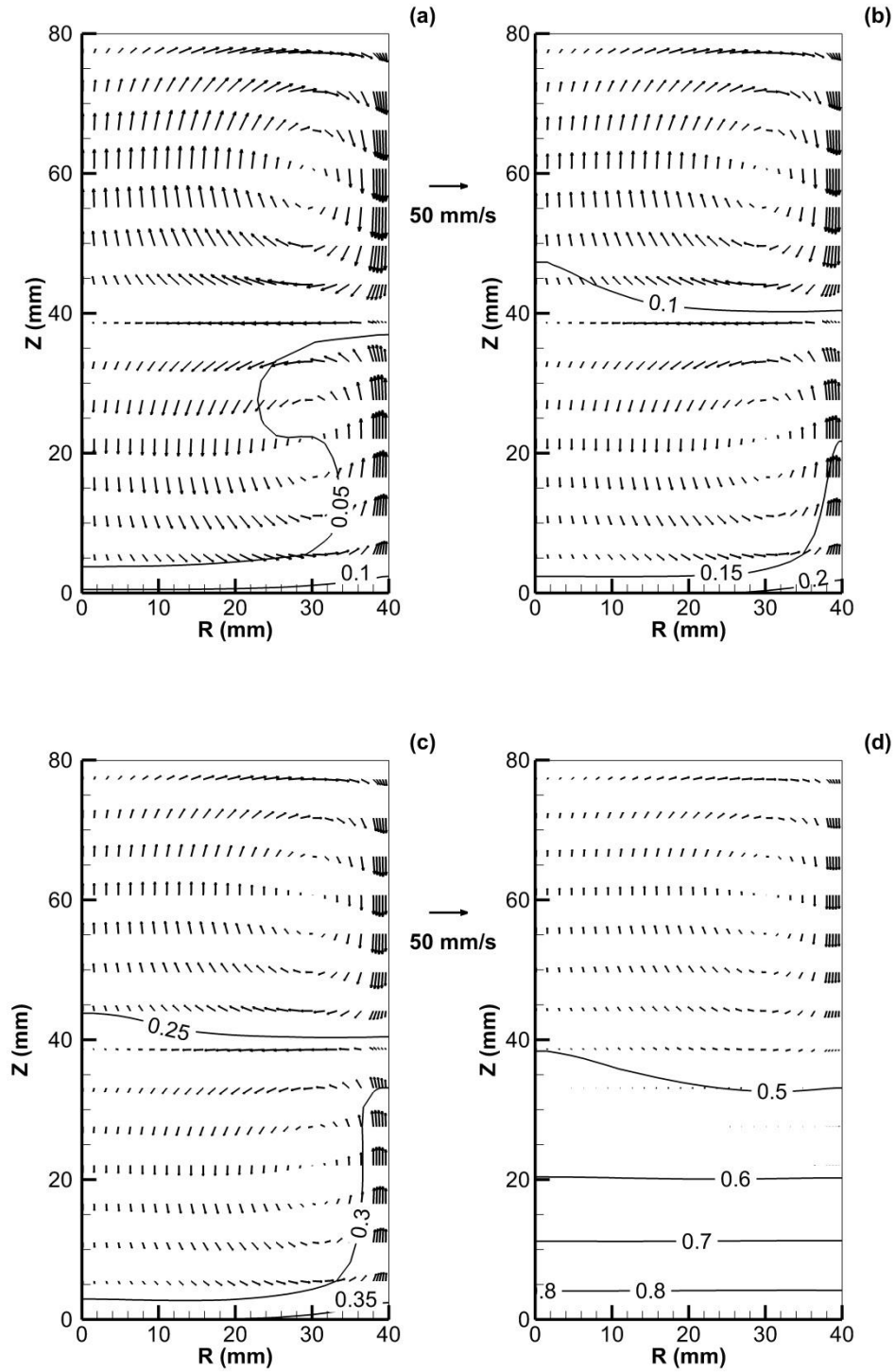


Figure 3.7—Computed velocity profiles in the metal at: (a) 30s, (b) 60s, (c) 120s, (d) 240s. Contours correspond to values of solid fraction.

Fig. 3.7(c) shows that damping of the flow is noticeable when solid fraction becomes greater than 0.25, with a characteristic velocity of 10 mm/s. The differences between the flow in the fixed particle region and the suspended particle region are clearly illustrated in Figure 3.7(d), which shows the flow characteristics after 240s. As seen in this figure, the flow in the fixed particle region is almost negligible compared with that of the suspended particle region. The velocity at the edge of the fixed/suspended particle regions is about 2 mm/s, and drops to 0.1 mm/s with increasing solid fraction. These results suggest that the velocity in the suspended particle region is quite large for EM stirred systems and cannot be ignored when describing heat and mass transfer phenomena. It should also be mentioned that this finding is a corollary to those reported by Oldenburg and Spera for strong thermosolutal convection in the mushy zone during solidification [12].

Figures 3.8(a) through 3.8(d) show the corresponding evolution of the turbulent field during solidification. At the beginning of solidification, Fig. 3.8(a), there is a marginal drop in the turbulent viscosity, particularly in the lower loop where solidification was initiated. The drop in the viscosity is more pronounced when the solid fraction is between 0.1 and 0.15, Fig. 3.8(b). Fig. 8(c) shows that turbulence is effectively damped after 120s, where solid fraction is around 0.3. The flow is completely laminarized as solid fraction approaches the coherency value, Fig. 3.8(d). It is interesting to see that the decay of turbulence occurs more rapidly than that of the velocity. This is expected, as the turbulent energy generation rate is proportional to the square of the velocity.

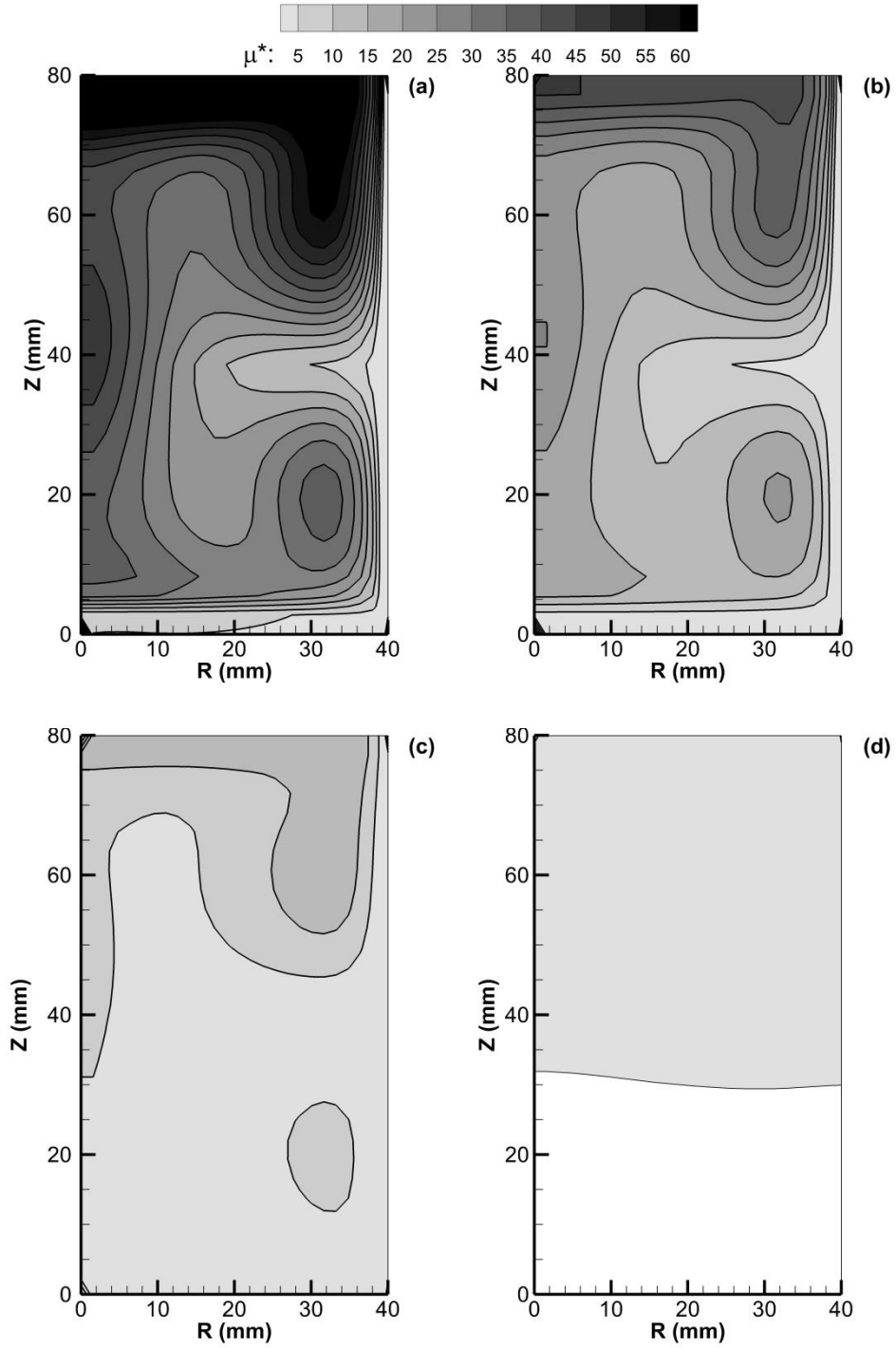


Figure 3.8—Computed turbulent-to-laminar viscosity in the metal at:
 (a) 30s, (b) 60s, (c) 120s, (d) 240s

It is instructive to compare the results of the presented model, which accounts for turbulent damping, with those which do not include such damping for EM stirred systems [20,21]. Figure 3.9 shows the variation of the velocity in the suspended particle region with respect to solid fraction. The values presented here have been normalized with respect to the velocity at zero solid fraction ($v^*=v/v_0$). This figure shows that ignoring the damping force does not lead to any change in the velocity until solid fraction is above 0.45. It should be mentioned that the sudden drop of the velocity near the coherency point is due to viscous effects at the boundary layer of the porous wall. This finding is particular to forced convection systems, where the external forces are relatively unaltered in the suspended particle region.

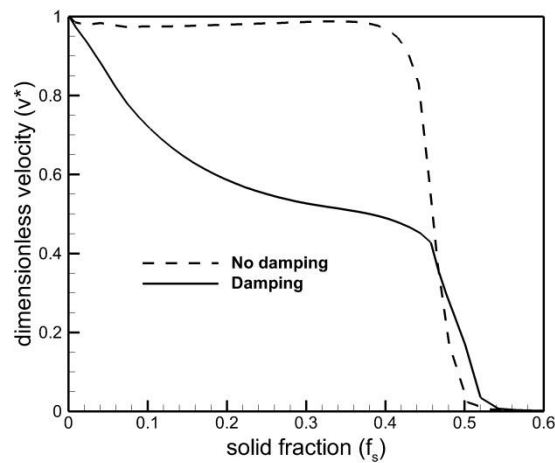


Figure 3.9—Comparison between the velocity in the suspended particle region with and without damping force

Figure 3.10 shows the variation of the turbulent viscosity versus solid fraction in the suspended particle region. This figure shows that the damping force causes the turbulent viscosity to decrease linearly with solid fraction across the suspended particle region. These results suggest that neglecting these interactions could lead to errors in computing the velocity

and turbulence levels in the mushy region, which could have profound effects on predicting solute segregation.

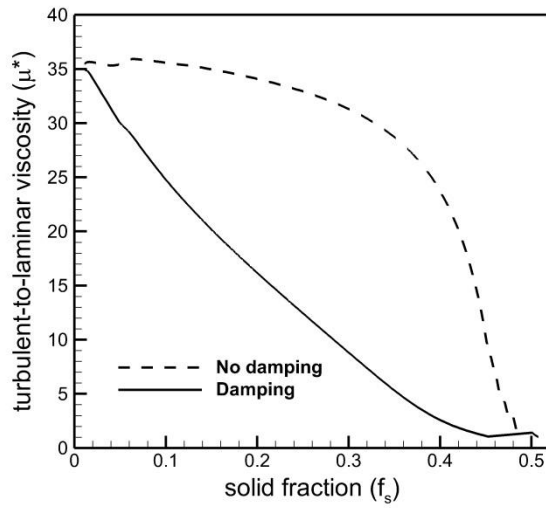


Figure 3.10—Comparison of turbulence in the suspended particle region with and without damping force

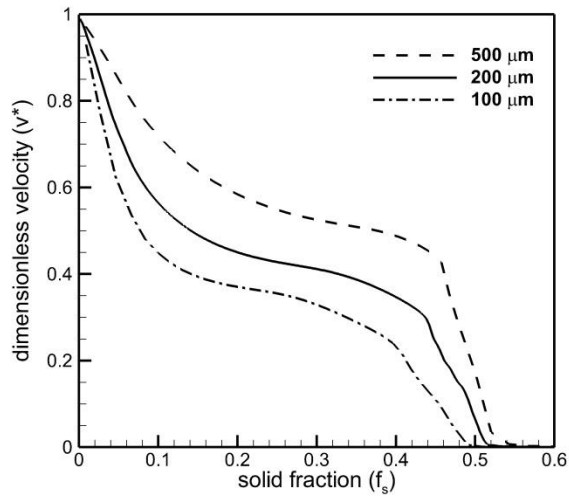


Figure 3.11—Influence of final grain size, D_g , on damping of velocity in the suspended particle region

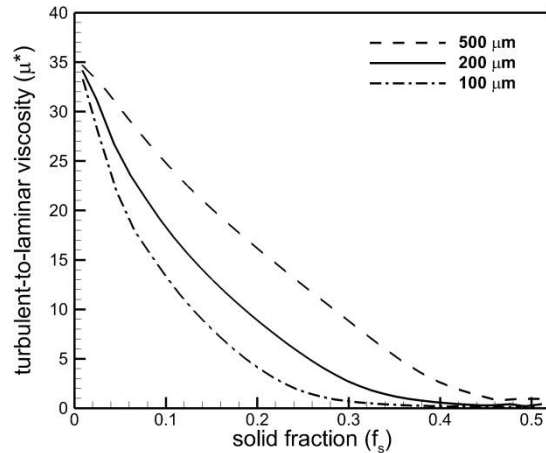


Figure 3.12—Influence of final grain size, D_g , on damping of turbulence in the suspended particle region

Since the damping force depends on the final grain size, it is interesting to examine its effect on the flow in the mushy zone. Figure 3.11 shows the variation of the velocity in terms of solid fraction for final grain sizes of 100, 200, and 500 μm . As seen in this figure, the velocity in the suspended particle region decays more rapidly for decreasing grain size. Figure 3.12 shows the corresponding variation of the turbulent viscosity as function of solid fraction in the suspended particle region. It should be noted that the decrease of the turbulent viscosity is faster than the velocity. These results suggest that the flow characteristics in the two-phase zone critically depend on both the solidification rate and nucleation potential of the melt, which dictate the grain size [36,37].

3.6—Conclusions

In this paper, an improved mathematical model has been presented for simulating electromagnetic, fluid flow, and heat transfer phenomena during solidification in an EM stirred system. The model allows for computation of the EM force field for any given coil

configuration, coil current, and coil frequency, and allows for the presence of magnetic shields. The solidification model is an extension of the dual-zone formulation to turbulent flows, and accounts for turbulent damping in the suspended particle region. An expression is presented describing the damping force in terms of turbulent kinetic energy, solid fraction, and final grain size.

This model was used to numerically investigate the electromagnetic field and evolution of the temperature and velocity fields to solidification in a bottom chill mold surrounded by an induction coil. The principal findings of this work are summarized as follows:

- The magnetic shields caused significant distortions in the EM force field near the base of the metal. This distortion affected the vorticity of the force field, which drives the flow. Such an effect necessitates numerical solution of the EM field.
- For melt stirring using a stationary magnetic field, the flow consisted of two axisymmetric, recirculating loops, and is highly turbulent. Solidification causes significant decay of the velocity and turbulent fields. The velocity decreases by one order of magnitude in the suspended particle region. Laminarization of the flow occurs in the middle of the suspended particle region for solid fraction around 0.3.
- The developed expression shows that the turbulent damping force depends on the final grain size. For smaller grains, the drop in the velocity occurs more rapidly with solid fraction.
- Neglecting the turbulent damping force led to a severe overestimation of both the velocity and turbulence levels in the suspended particle region.

The paper presented here represents a more comprehensive model for EM solidification processes. It allows for the calculation of the electromagnetic field to permit a more realistic description of the flow in the solidification system. It also provides a model for describing turbulent flow behavior in the mushy region. These improvements to existing models offer a framework for better understanding the roles of fluid flow and heat transfer phenomena on solidification in both EM stirring and other forced convection systems.

3.7—Acknowledgement

The authors graciously thank the National Science Foundation for their funding of this project under grant CMMI-0856320.

3.8—References

- [1] A.A. Tzavaras and H.D. Brody: *J. Met.*, 1984, vol. 36, no. 3, pp. 31-37.
- [2] C. Vives: in *Magneto hydrodynamics in Process Metallurgy*, eds. J. Szekely, J.W. Evans, K. Blazek, and N. El-Kaddah, pp. 169-174, TMS, Warrendale, PA, 1991.
- [3] Y.A. Kompan, I. Protokovilov, Y. Fautrelle, Y.U. Gelfgat, and A. Bojarevics: in *Modelling for Materials Processing*, pp. 85-90, University of Latvia Press, Riga, 2010.
- [4] C. Vives and C. Perry: *Int. J. Heat Mass Transfer*, 1986, vol. 29, pp. 21-33.
- [5] Q. Zhao, X. Zhang, C. Feng, N. Zhang, Y. Han, J. Guo, and X. Hou: *Adv. Mater. Res.*, 2012, vols. 482-484, pp. 1447-1452.
- [6] K.A. Jackson, J.D. Hunt, and D.R. Uhlmann: *Trans TMS-AIME*, 1966, vol. 236, pp. 149-158.
- [7] B. Willers, S. Eckert, U. Michel, I. Haase, G. Zouhar: *Mater. Sci. Eng. A*, 2005, vol. 402, pp. 55-65.
- [8] J.A. Dantzig and M. Rappaz: *Solidification*, pp. 464-466, EPFL Press, Lausanne, 2009.
- [9] B. Wang, Y. Yang, and W. Tang: *Trans. Nonferrous Met. Soc. China*, 2008, vol. 18, pp. 536-540.
- [10] B. Chalmers: *J. Aust. Inst. Met.*, 1963, vol. 8, pp. 255-263.

- [11] R. Mehrabian, M. Keane, and M.C. Flemings: *Metall. Trans.*, 1970, vol. 1, pp. 455-464.
- [12] C.M. Oldenburg and F.J. Spera: *Numer. Heat Transfer, Part B*, 1992, vol. 21, pp. 217-229.
- [13] C.J. Parides, R.N. Smith, and M.E. Glicksman: *Metall. Trans. A*, 1997, vol. 28, pp. 875-883.
- [14] T. Campanella, C. Charbon, and M. Rappaz: *Scr. Mater.*, 2003, vol. 49, pp. 1029-1034.
- [15] P.J. Prescott and F.P. Incropera: *J. Heat Transf.*, 1995, vol. 117, pp. 716-724.
- [16] P.J. Prescott and F.P. Incropera: *J. Heat Transf.*, 1993, vol. 115, 302-310.
- [17] W. Shyy, Y. Pang, G. Hunter, D.Y. Wei, and M.H. Chen: *Intl. J. Heat Mass Transf.*, 1992, vol. 35, 1229-1245.
- [18] W. Shyy, Y. Pang, G. Hunter, D.Y. Wei, and M.H. Chen: *ASME J. Eng. Mater. Technol.*, 1993, vol. 115, 8-16.
- [19] R. Lantzsch, V Galindo, I. Grants, C. Zhang, O. Paetzold, G. Gerbeth, and M. Stelter: *J. Crystal Growth*, 2007, vol. 305, 249-256.
- [20] R. Pardeshi, A.K. Singh, and P. Dutta: *Numer. Heat Transfer, Part A*, 2008, vol. 55, pp. 42-57.
- [21] O. Budenkova, F. Baltaretu, J. Kovács, A. Roósz, A. Rónaföldi, A.M. Bianchi, and Y. Fautrelle: *IOP Conf. Ser.: Mater. Sci. Eng.*, 2012, vol. 33, 012046.
- [22] Y. Yamagishi, H. Takeuchi, A.T. Pyatenko, and N. Kayukawa: *AIChE J.*, 1999, vol. 45, pp. 696-707.
- [23] J.L. Alvarado, C. Marsh, C. Sohn, G. Phetteplace, and T. Newell: *Int. J. Heat Mass Transfer*, 2007, vol. 50, pp. 1938-1952.
- [24] S. Wenji, X. Rui, H. Chong, H. Shihui, D. Kaijun, and F. Ziping: *Int. J. Refrig.*, 2009, vol. 32, pp. 1801-1807.
- [25] E. Kolbe and W. Reiss: *Wiss. Z. der TH Ilmenau*, 1963, vol. 9, 311-317.
- [26] R.F. Dudley and P.E. Burke: *IEEE Trans. Indu. Appl.*, 1972, vol. 8, 565-571.
- [27] N. El-Kaddah and J. Szekely: *J. Fluid Mech.*, 1983, vol. 133, 37-46.
- [28] J.L. Meyer, N. El-Kaddah, J. Szekely, C. Vives, and R. Ricou: *Metall. Trans. B*, 1987, vol. 18, 529-538.
- [29] H. Tennekes and J.L. Lumley: *A First Course in Turbulence*, pp. 19-20, MIT Press, Cambridge, 1972.
- [30] W. P. Jones and B.E. Launder: *Int. J. Heat Mass Transfer*, 1972, vol. 15, pp. 301-314.

- [31] D.G. Thomas: *J. Colloid Sci.*, 1965, vol. 20, pp. 267-277.
- [32] P. Bradshaw, D.H. Ferriss, and N.P. Atwell: *J. Fluid Mech.*, 1967, vol. 28, pp. 593-616.
- [33] B.E. Launder and D.B. Spalding: *Mathematical Models of Turbulence*, p. 78, Academic Press, London, 1972.
- [34] W.M. Pun and D.B. Spalding: Report HTS/76/2, Imperial College of Science and Technology, London, August 1977.
- [35] S.V. Patankar: *Numerical Heat Transfer and Fluid Flow*, Hemisphere Publishing, New York, 1980.
- [36] G. Poole, N. Rimkus, A. Murphy, P. Boehmcke, and N. El-Kaddah: in *Magnesium Technology 2012*, eds. S.N. Mathaduhu, W.H. Sillekens, N.R. Neelmeggham, and N. Hort, pp. 161-164, Wiley, New York, 2012.
- [37] L. Nastac and N. El-Kaddah: *IOP Conf. Ser.: Mater. Sci. Eng.*, 2012, vol. 33, 012084.

Appendix 3A—The Damping Force in the Suspended Particle Region

In the suspended particle region, the fluctuating velocity of the solid particles is zero, and the instantaneous velocity of the two-phase mixture is

$$\mathbf{u} = \bar{\mathbf{u}} + \mathbf{u}' = f_L (\bar{\mathbf{u}}_L + \mathbf{u}'_L) + f_s \mathbf{u}_s \quad [\text{A3-1}]$$

The instantaneous Navier-Stokes equation in this region can then be written as

$$\begin{aligned} \frac{\partial \left(\rho \left(f_s \bar{\mathbf{u}}_s + f_L (\bar{\mathbf{u}}_L + \mathbf{u}'_L) \right) \right)}{\partial t} \\ + \nabla \cdot \left(\rho \left(f_s \bar{\mathbf{u}}_s + f_L (\bar{\mathbf{u}}_L + \mathbf{u}'_L) \right) \left(f_s \bar{\mathbf{u}}_s + f_L (\bar{\mathbf{u}}_L + \mathbf{u}'_L) \right) \right) \\ = -\nabla (\bar{p} + p') + \mu_t \nabla^2 \left(f_s \bar{\mathbf{u}}_s + f_L (\bar{\mathbf{u}}_L + \mathbf{u}'_L) \right) + \mathbf{F}_{em} \end{aligned} \quad [\text{A3-2}]$$

Taking the time average of (A3-2) yields

$$\frac{\partial (\rho \bar{\mathbf{u}})}{\partial t} + \nabla \cdot (\rho \bar{\mathbf{u}} \bar{\mathbf{u}}) + \nabla \cdot (f_L^2 \bar{\boldsymbol{\tau}}_t) = -\nabla \bar{p} + \mu_t \nabla^2 \bar{\mathbf{u}} + \mathbf{F}_{em} \quad [\text{A3-3}]$$

where $\boldsymbol{\tau}_t$ is the Reynolds stress tensor. From Eqs. (3-11) and (A3-3), the damping force is given

by

$$\mathbf{F}_D = (1 - f_L^2) \nabla \cdot \bar{\boldsymbol{\tau}}_t \quad [\text{A3-4}]$$

Chapter 4

The Effect of Coil Design on the Temperature and Velocity Fields during Solidification in Electromagnetic Stirring Processes

4.1—Abstract

This paper examines the role of induction coil design on stirring of molten metal in electromagnetic (EM) solidification processes. A model is presented to describe the EM, heat transfer, and fluid flow phenomena in these processes. It is based on a dual-zone description of the mushy region, and accounts for damping of turbulence by the solidified crystallites. The electromagnetic field equations were solved using the mutual inductance technique, while the temperature and turbulent flow fields were calculated using the control volume method. Calculations were performed for solidification of an Al-Cu alloy placed in a stationary magnetic field generated by an induction coil. The effect of coil design on the flow structure was investigated for three different coil positions. It was found that changing the coil position significantly alters the flow pattern from four recirculating loops when the coil is above the midsection of the melt to two loops, typical of a travelling magnetic field, when the coil is at the base of the melt. This significantly modifies the rate of solidification across the ingot, as well as the temperature gradient, in the mushy region. The decay of the velocity and turbulent fields in the mushy region was found to be exponential, with the maximum rate of decay at the solidification front. These results indicate that through changes in coil design, it is possible to control the flow characteristics and solidification behavior in the molten metal.

4.2—Introduction

Electromagnetic stirring technologies have found extensive use in solidification processing of metals as a means to produce castings exhibiting fine-grained equiaxed structure. The flow serves to minimize thermal gradients in the molten pool¹⁾ and rapidly dissipates the melt superheat²⁾, which in turn promotes an early occurrence of the columnar-to-equiaxed transition^{3,4)}. In addition, it increases fragmentation of the secondary dendrite arms, leading to a higher nucleation potential in the melt^{1,5,6)}. Clearly, understanding flow characteristics of electromagnetically-stirred melt in the mushy zone is critical in order to control the grain structure of cast alloys.

Electromagnetic (EM) stirring is generally accomplished by induction from a time-varying magnetic field using a suitable induction coil. The passage of an alternating current induces eddy currents in the melt, which are dissipated as heat (Joule heating). Also, the interaction between the induced current and the applied magnetic field produces EM forces, which drive the flow in the melt. The flow behavior in EM stirred melts is generally controlled by the applied magnetic field used, namely stationary^{2,7,8)}, rotating⁹⁾, or traveling magnetic fields^{5,10)}. Moreover, the resulting flow field is highly sensitive to variations in coil design, namely the coil configuration^{11,12)} and the location of the coil with respect to the melt^{13,14)}.

During past decades, extensive work exemplified by those of Evans^{15,16)}, Fautrelle^{17,18)}, Szekely¹⁹⁾, and El-Kaddah^{10,20)} has led to a reasonably good level of understanding of the key flow phenomena in EM stirred melts. Their models involve solution of the Maxwell and turbulent Navier-Stokes equations to describe the electromagnetic and velocity fields in the liquid metal. However, implementation of this approach to solidification processes is somewhat complicated due to the difficulties associated with the presence of the two-phase mushy zone.

There are two models for describing the flow in the mushy zone, namely single-zone^{7,21,22)} and dual-zone models^{23,24)}. The single-zone model treats the entire two-phase region as a porous medium, with the flow being damped via Darcy's law. The dual-zone model divides the mushy zone into two domains: (i) the suspended particle region, and (ii) the fixed particle region, with the transition between regions occurring at the coherency point. In modeling EM solidification processes, the former model was used by Rappaz and coworkers⁷⁾ and Prescott and Incropera²²⁾, while the latter was used by Pardeshi et al²⁴⁾. In all of these studies, an approximate analytical solution was used to describe the EM force field, which limited their ability to address the role of the coil design on the solidification behavior.

Recently a new dual-zone solidification model has been proposed by the authors²⁵⁾ for EM stirred flows. This model includes numerical solution of the EM field, using the coil geometry and operating conditions as fundamental input parameters. The model also accounts for the damping of turbulence, a characteristic of EM stirred flows, in the two-phase mushy zone due to interactions between the turbulent eddies and the solid crystallites. This paper investigates the influence of coil design on the flow characteristics for a single-phase induction coil.

4.3—Model Formulation

The mathematical description of the problem for any EM stirred solidification system is readily given in terms of the continuity, momentum, and heat transfer equations, along with appropriate subsidiary relationships defining the electromagnetic force field, heat generation, and turbulence parameters in the system. This formulation will be given in broad outline only. Detailed derivation of the model equations are given in reference²⁶⁾. Further elaboration on the steps in modeling such systems may be found in other references^{8,10,18)}.

4.3.1—Formulation of the Electromagnetic Field Problem

To allow for the presence of magnetic shields (chill block) and arbitrary coil configuration, it is convenient to use the mutual inductance method for two dimensional systems. In this method, the conducting region(s), with electrical conductivity σ , is divided into a number of elementary circuits with constant current density, \mathbf{J} . The current density in each circuit is given by

$$\oint \mathbf{J} \cdot d\mathbf{l}_i = -j\omega\sigma \left[\sum_{m=1}^{metal} M_{i,m} (\mathbf{J} \cdot \mathbf{S})_m + \sum_{c=1}^{shields} M_{i,c} (\mathbf{J} \cdot \mathbf{S})_c + \sum_{k=1}^{coil} M_{i,k} I_k \right] \quad [4-1]$$

where \mathbf{S} and \mathbf{l} are the respective lengths and surface areas of the elementary circuits, j is the square root of -1, ω is the angular frequency, and $M_{i,j}$ is the mutual inductance given by

$$M_{i,k} = \frac{\mu_0}{4\pi} \oiint \frac{d\mathbf{l}_k \cdot d\mathbf{l}_i}{r'} \quad [4-2]$$

From the current density, the magnetic flux density, \mathbf{B} , Joule heating, q_{em} , and EM force field, F_{em} , are respectively determined by the following relations:

$$\mathbf{B} = -\frac{\nabla \times \mathbf{J}}{j\omega\sigma} \quad [4-3]$$

$$S_{em} = \frac{1}{2} \text{Re} \left(\frac{\mathbf{J} \cdot \mathbf{J}^*}{\sigma} \right) \quad [4-4]$$

where the asterisk denotes the complex conjugate.

4.3.2—Formulation of the Heat Transfer Problem

Assuming that solid fraction, f_s , varies linearly with temperature, the differential equation representing the energy balance with phase change as a result of solidification may be written as:

$$\rho C^* \frac{DT}{Dt} = \nabla \cdot (k^* \nabla T) + S_{em} \quad [4-5]$$

where C^* is the effective specific heat given in terms of the specific heat c_p , latent heat L , and the solidus and liquidus temperatures, T_S and T_L , respectively, by

$$C^* = \begin{cases} c_{p,l} & T \geq T_L \\ c_{p,s} + \frac{L}{T_L - T_S} & T_S < T < T_L \\ c_{p,s} & T \leq T_S \end{cases} \quad [4-6]$$

In Equation (4-6), the l and s subscripts correspond to values for the liquid and solid phases, respectively. In convective turbulent flows, the effective thermal conductivity, k^* , in the bulk liquid, mushy zone, and solidified metal is given by:

$$k^* = \begin{cases} k_l + \frac{\mu_t c_{p,l}}{\text{Pr}} & T \geq T_L \\ (1 - f_s)k_l + f_s k_s & T_S \leq T < T_L \\ k_s & T \leq T_S \end{cases} \quad [4-7]$$

For bulk liquids ($T > T_L$), the effective thermal conductivity is given by the sum of the turbulent and molecular thermal conductivities, where μ_t and Pr are the turbulent viscosity and turbulent Prandtl number, respectively. In the mushy zone, the conductivity is a weighted sum of the solid and effective liquid conductivities. In the solidified metal, the conductivity is equal to the conductivity of the solid.

4.3.3—Formulation of the Fluid Flow Problem

For the three flow domains, namely the bulk liquid, suspended particle, and fixed particle regions, the continuity and Navier-Stokes equations can be expressed as:

Continuity:

$$\nabla \cdot \mathbf{u} = 0 \quad [4-8]$$

where

$$\mathbf{u} = f_s \mathbf{u}_s + (1 - f_s) \mathbf{u}_l \quad [4-9]$$

Navier-Stokes:

$$\rho \frac{\partial \mathbf{u}}{\partial t} + \rho \mathbf{u} \cdot \nabla \mathbf{u} = -\nabla P + \mu \nabla^2 \mathbf{u} + \lambda (\mathbf{F}_{em} + \mathbf{F}_d) - \frac{\mu_t}{K} (\mathbf{u} - \mathbf{u}_s) \quad [4-10]$$

where \mathbf{F}_{em} , \mathbf{F}_d , K , and λ represent the bulk electromagnetic force, turbulent damping force, permeability, and a switch parameter, respectively. For the suspended particle region, λ is equal to unity and is zero in the fixed particle region. Since it is assumed that the velocity of solid is equal to velocity of liquid in the bulk and suspended particle region, the permeability term is finite only in the fixed particle region. In this study, the permeability was determined using the Carman-Kozeny equation.

In this work, it is assumed that the flow in the fixed particle region is laminar. This assumption is reasonable, as the interparticle spacing in this region is on the order of the Kolomogrov turbulence length scale. For the bulk liquid and suspended particle regions, the turbulent characteristics of the flow are defined by the low-Re k- ε model²⁷. The governing equations for the turbulent kinetic energy, k , and the turbulent energy dissipation, ε , are:

k-equation

$$\rho \frac{\partial k}{\partial t} + \rho \mathbf{u} \cdot \nabla k = \nabla \cdot \left(\frac{\mu_t}{P_k} \nabla k \right) + G_{ij} - \rho \varepsilon \quad [4-11]$$

ε -equation

$$\rho \frac{\partial \varepsilon}{\partial t} + \rho \mathbf{u} \cdot \nabla \varepsilon = \nabla \cdot \left(\frac{\mu_t}{P_\varepsilon} \nabla \varepsilon \right) + C_1^* G_{ij} \frac{\varepsilon}{k} - C_2^* \rho \frac{\varepsilon^2}{k} \quad [4-12]$$

where C_1^* and C_2^* are constants. The turbulent viscosity is defined by

$$\mu_t = C_\mu^* \rho \frac{k^2}{\varepsilon} \quad [4-13]$$

where C_μ^* is a constant. The effective viscosity is the sum of the laminar and turbulent components. For the bulk liquid and fixed particle region, the laminar viscosity is equal to its molecular value. In the suspended particle region, the laminar viscosity is determined from rheological behavior using the expression of Thomas²⁸⁾.

4.3.4—Turbulent Damping Model

The turbulent damping force in the suspended particle region is

$$\mathbf{F}_d = (1 - f_L^2) \nabla \cdot \bar{\tau}_t \quad [4-14]$$

where τ_t is the turbulent Reynolds stress. It is assumed that the turbulent stress is isotropic and proportional to the turbulent kinetic energy. Therefore, the divergence term in Equation (4-14) is equal to

$$\nabla \cdot \bar{\tau}_t = c_d^{1/2} \rho \nabla k \quad [4-15]$$

where c_d is a constant equal to 0.08²⁹⁾. In Equation (4-15), the turbulent grad term is equal to the difference in turbulent kinetic energy between the liquid and the crystallite surface, where k is taken to be zero. For a simple cubic arrangement of crystallites of size d with distance between vertices D_f , the grad term may be approximated by:

$$\nabla k = \frac{2k}{(D_g - d)} \hat{\mathbf{e}}_j \quad [4-16]$$

To determine instantaneous particle size, the solid fraction of the cell is given by

$$f_s = \frac{\pi d^3 \beta}{6D_g^3} \quad [4-17]$$

where β corresponds to the ratio of the particle volume to the volume of the spherical envelope of the crystallite. For spherical particles, β is equal to unity. Rearranging gives:

$$d = \gamma D_g f^{1/3} \quad ; \quad \gamma = \left(\frac{6}{\pi \beta} \right)^{1/3} \quad [4-18]$$

From Equations (4-14)-(4-16) and Equation (4-18), the damping force can be given in terms of solid fraction by:

$$\mathbf{F}_d = \frac{2(f_s^2 - 2f_s)\sqrt{c_d \rho k}}{D_g(1 - \gamma f_s^{1/3})} \hat{\mathbf{e}}_j \quad [4-19]$$

It should be noted that in previous formulations²⁵⁾ the turbulent damping force was given in terms of the coherency solid fraction. From Equation (4-18), it can be seen that the coherency is equal to $1/\gamma^3$. For spherical particles, the coherency solid fraction is equal to 0.521.

4.4—Solution Technique

In the calculation of the magnetic field, the metal and adjacent conducting regions were divided into a number of elementary circuits. A finer grid was used near the outer radius of the conducting domains to accurately describe the decay of the magnetic field in the skin depth. The current density in each elementary circuit was calculated solving the set of \mathbf{J} equations using Choleski factorization method. Upon obtaining the \mathbf{J} field, the magnetic flux density \mathbf{B} was evaluated from Ampere's law. These two fields were then used to calculate the electromagnetic force field and Joule heating.

In this work, the control volume technique³⁰⁾ was used to solve the equations for the temperature, fluid flow, and turbulent fields. In this technique, a mesh divides the metal solution domain into a number of contiguous volume elements. The equations were discretized over each individual control volume, and the resulting discretized equations were solved iteratively using tri-diagonal algorithm technique TDMA. In the calculation of the velocity field the SIMPLE algorithm was used³¹⁾.

4.5—Results and Discussion

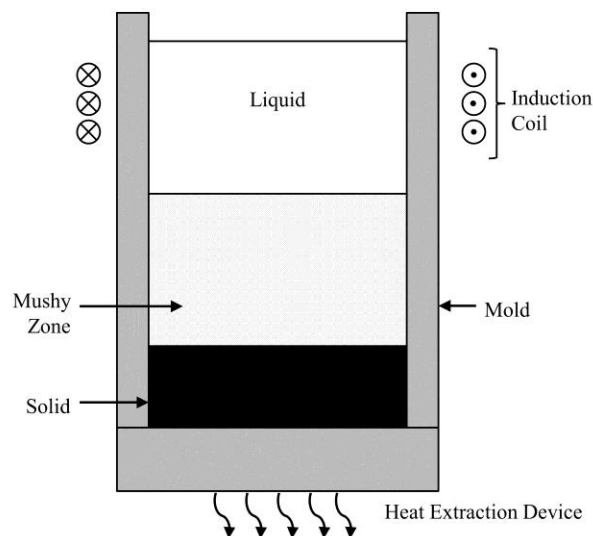


Figure 4.1 Sketch of unidirectional EM solidification system.

In this section, we shall present the effect of coil design on the computed velocity and temperature fields during solidification. This study focuses on the influence of the coil position on the flow and solidification phenomena. The calculations were carried out for unidirectional solidification of Al-Cu alloy in a bottom chill mold surrounded by an induction coil, as shown in Figure 4.1. The solidus and liquidus temperatures are 564 and 648 °C, respectively. The inner diameter of the mold and metal height were 80 mm, respectively, and the thickness of the

stainless steel chill block was 80 mm. A three turn coil of diameter 130 mm, with a spacing of 10 mm between each turn, was used in these calculations. Three coil positions were examined, and were chosen such that the coil center was aligned with the top, middle, and bottom of the melt. Stirring of the molten metal during solidification was carried out for a coil current of 200 A, and a frequency of 500 Hz. In this study, the crystallites were assumed to be spherical ($\beta=1$), which corresponds to globular solidification morphology, and the final grain size, D_f , was taken to be 200 μm .

Figures 4.2(a-c) show the initial flow field for the three coil positions considered. These figures show that the coil location has a substantial effect on the flow pattern. The flow corresponding to the middle coil position, typically used in induction stirring, is characterized by two recirculating loops of equal size, Figure 4.2a. Placing the coil at the top and bottom of the melt drastically changes the flow pattern, Figures 4.2b and 4.2c, respectively. When the coil is located at the top, the lower loop grows considerably in size at the expense of the upper loop, while the flow for the bottom coil position is characterized by essentially one loop similar to those typically found for traveling magnetic fields¹⁰. Here it should be mentioned that when the coil is above the midplane of the melt, the flow in the upper loop is clockwise, and is counterclockwise in the lower loop. For the bottom coil position, the flow is opposite that of the middle and top positions at the metal/chill interface. These results suggest that the coil location can be used to control the flow directionality in the melt.

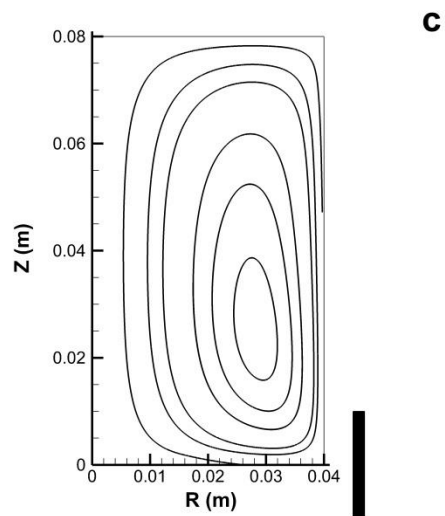
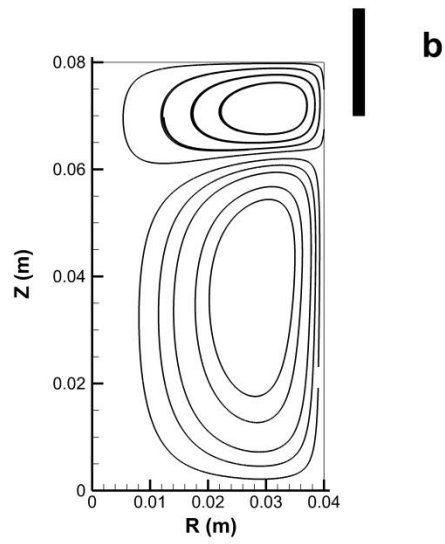
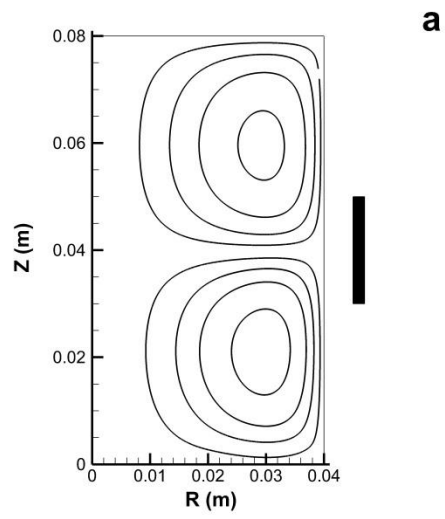


Figure 4.2 Initial flow patterns at different coil locations: (a) middle, (b) top, and (c) bottom

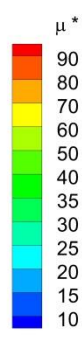
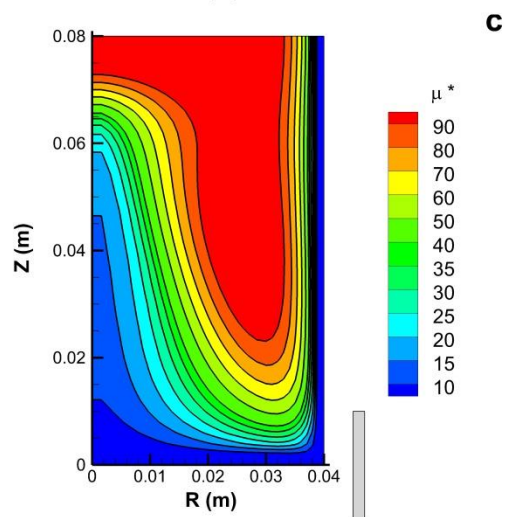
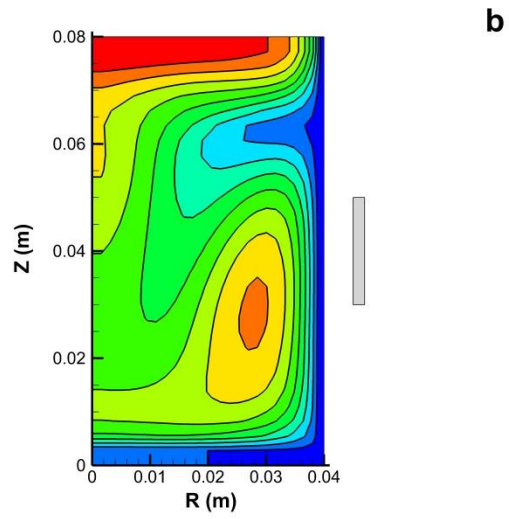
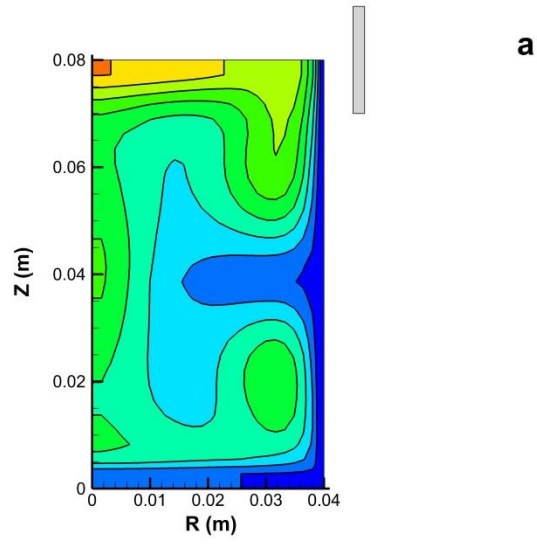


Figure 4.3 Initial turbulent fields at different coil positions: (a) middle, (b) top, and (c) bottom

The coil position also affects the turbulent characteristics of the flow. Figures 4.3(a-c) show the turbulent viscosity, normalized with respect to the laminar viscosity ($\mu^* = \mu_t / \mu_l$), for the middle, top, and bottom coil positions, respectively. The turbulent field for the middle coil position, Figure 4.3(a), is essentially symmetrical, with the maximum values of turbulent viscosity being found where the shear strain rates are highest, namely the vortex centers and the free surface. By placing the coil at the top of the metal, where the flow is characterized by two unequal recirculating loops, the turbulent viscosity is higher than that for the middle coil position. Furthermore, the maximum values of turbulent viscosity are located in the vortices of each loop, Figure 4.3(b). When the coil is placed at the base of the melt, where the flow is characterized by a single loop, the spatial variation of the turbulent viscosity is completely different compared to that of the other two coil positions. Turbulence is more intense, and is more or less uniform throughout the melt, Figure 4.3(c). Since the flow affects the temperature field in both the liquid and mushy regions, these results suggest that the coil location has a strong influence on the solidification rate.

The changes in solidification rate with the coil position are illustrated in Figures 4.4(a-c). These figures show the velocity and temperature fields after 120s of solidification for the middle, top, and bottom coil positions, respectively. It is seen that stirring changes the solidification behavior from unidirectional to non-uniform, as indicated by the radial variation of temperature in the mushy region. Furthermore, the local rate of solidification depends on the direction of the flow. Inspection of these figures shows that when the flow travels away from the chill plate, the rate of solidification is higher, and is depressed when the flow is travelling downward as a result of remelting of the solidification front.

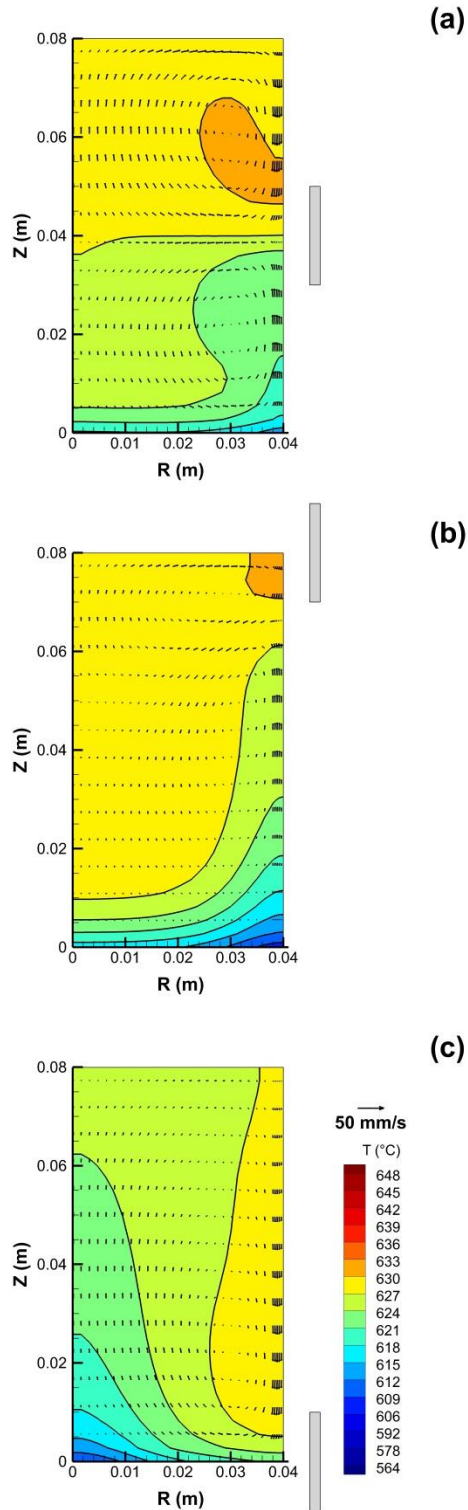


Figure 4.4 Computed velocity and temperature fields in the suspended particle region after 120s: (a) middle; (b) top; and (c) bottom coil positions.

The dependence of the solidification rate on the flow field is reflected in the obtained changes of solidification rate across the melt with coil location. For the top coil position, the maximum rate of solidification is near the mold wall, while it is at the centerline of the metal for the bottom coil position. This point is further illustrated in Figure 4.5, which shows the radial temperature variation for the top and bottom coil positions at $z=20$ mm. As seen in this figure, the temperature at the centerline is at a maximum for the bottom coil position and decreases across the melt, while it is at a minimum for the top coil position and increases along the radius.

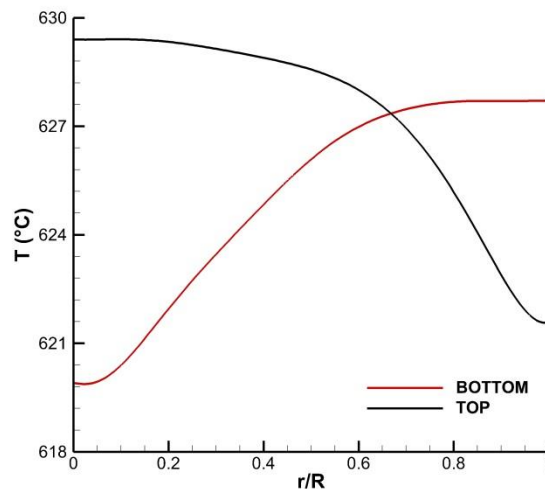


Figure 4.5 A comparison of the radial temperature distributions for the top and bottom coil positions after 120s ($z=20$ mm).

Since the convective heat flux depends on the velocity and turbulent intensity, it is instructive to examine the effect of coil location on the decay of the flow field. As seen in Figures 4.5(a-c), the coil position has little effect on the magnitude of the velocity in the suspended particle region. The decay in the magnitude of the velocity during solidification is shown in Figure 4.6. As seen in this figure, the flow in the suspended particle region decays rapidly in the initial stages of solidification up to solid fraction 0.1, and the rate of decay

decreases as solidification progresses. Furthermore, the rate of decay is essentially independent of the coil position, except near the interface between the suspended and fixed particle regions.

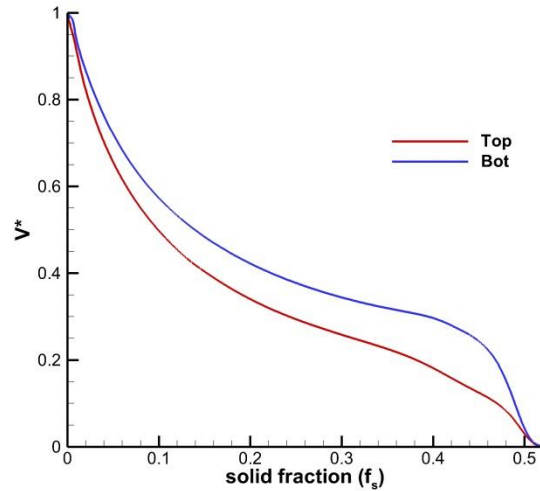


Figure 4.6 Decay of velocity in the suspended particle region for top and bottom coil positions ($r=20$ mm, $z=30$ mm).

Figure 4.7 shows the corresponding decay of the turbulent viscosity normalized with respect to the laminar value. It is seen that the decay behavior of the turbulent viscosity is similar to that of the velocity. From these results, it is apparent that the coil position has little or no effect on the overall rate of solidification in the metal. These findings are consistent with the cooling rate measurements by Campanella et al for different coil positions⁶⁾.

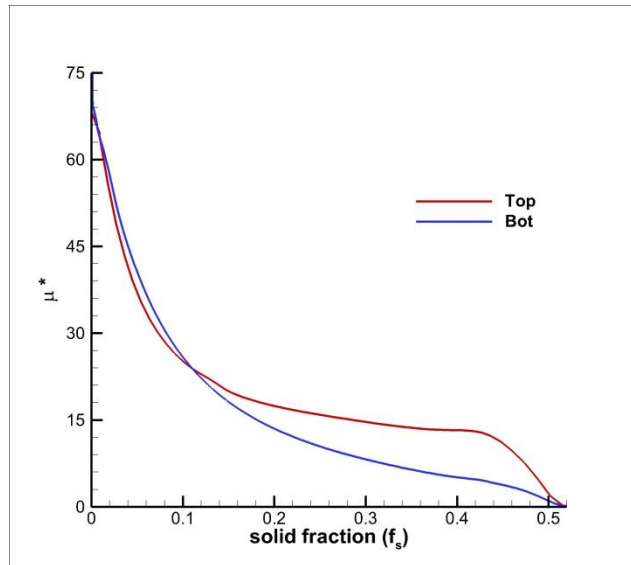


Figure 4.7 Decay of turbulent-to-laminar viscosity ratio in the suspended particle region for top and bottom coil positions ($r=20$ mm, $z=30$ mm).

4.6—Conclusions

A mathematical model for EM stirred solidification processes has been developed. The presented solidification model is based on the numerical solution of the electromagnetic field equations using the mutual inductance method, and extends the dual-zone velocity and temperature field models to incorporate turbulent flow. The model also accounts for the damping of turbulence at the crystallite surfaces. The model provides a vivid description of the evolution of the various electromagnetic, heat transfer, and flow phenomena in the system during solidification. Furthermore, the model contains the flexibility such that it can describe these phenomena for any coil configuration, position, and operating conditions, making it a powerful tool in the analysis and/or design of EM solidification processes.

The model was used to investigate the effect of coil location on the flow and temperature evolution during solidification in a stationary magnetic field. The results of this study shows that the coil position significantly modifies the flow pattern in the melt, and alters the directionality of the flow in the bulk liquid. The coil location was also found to affect the local solidification

rate. It was also found that the decay of the velocity and turbulent viscosity primarily occurs in the earliest stages of solidification ($f_s < 0.1$), and is independent of coil position. It is hoped that the model presented in this work will provide a sound theoretical framework and will allow for a more in-depth understanding of EM stirring during solidification and for precise control of the flow structure in EM stirred systems.

4.7—References

- [1] B. Willers, S. Eckert, U. Michel, I. Haase and G. Zouhar: *Mater. Sci. Eng. A*, **402**(2005), 55.
- [2] C. Vivés and C. Perry: *Intl. J. Heat Mass Transf.*, **29**(1986), 21.
- [3] B. Chalmers: *J. Aust. Inst. Met.*, **8**(1963), 255.
- [4] J.A. Dantzig and M. Rappaz: Solidification, EPFL Press, Lausanne, (2009), 458.
- [5] W. Griffiths and D. McCartney: *Mater. Sci. Eng. A*, **216**(1996), 47.
- [6] T. Campanella, C. Charbon and M. Rappaz: *Metall. Mater. Trans. A*, **35**(2004), 3201.
- [7] T. Campanella, C. Charbon and M. Rappaz: *Scripta Mater.*, **49**(2003), 1029.
- [8] N. El-Kaddah and J. Szekely: *J. Fluid Mech.*, **133**(1983), 37.
- [9] V. Travnikov, P.A. Nikrityuk, K. Eckert, D. Rübiger, S. Odenbach and S. Eckert: *IOP Conf. Ser.: Mater Sci. Eng.*, **33**(2012), 012048.
- [10] N. El-Kaddah, J. Szekely and G. Carlsson: *Metall. Trans. B*, **15**(1984), 633.
- [11] J.W. McKelliget and N. El-Kaddah: *J. Appl. Phys.*, **64**(1986), 2948.
- [12] V. Bojarevics, K. Pericleous and M. Cross: *Metall. Mater. Trans. B*, **31**(2000), 179.
- [13] V. Bojarevics, A. Roy and K.A. Pericleous: *Magnetohydrodyn.*, **46**(2010), 317.
- [14] C. Stelian, Y. Delannoy, Y. Fautrelle and T. Duffar: *J. Cryst. Growth*, **275**(2005), 1571.
- [15] E.D. Tarapore and J.W. Evans: *Metall. Trans. B*, **7**(1976), 343.
- [16] E.D. Tarapore, J.W. Evans and J. Langfeldt: *Metall. Trans. B*, **8**(1977), 179.
- [17] Y. Fautrelle: *J. Fluid Mech.*, **102**(1981), 405.

- [18] N. El-Kaddah, J. Szekely, E. Taberlet and Y. Fautrelle: *Metall. Trans. B*, **17**(1986), 687.
- [19] K. Nakanishi, T. Fujii and J. Szekely: *Ironmak. Steelmak.*, **2**(1975), 193.
- [20] J.L. Meyer, J. Szekely and N. El-Kaddah: *Trans. ISIJ*, **27**(1987), 25.
- [21] R. Mehrabian, M. Keane and M.C. Flemings: *Metall. Trans.*, **1**(1970), 455.
- [22] P.J. Prescott and F.P. Incropera: *J. Heat Transf.*, **117**(1995), 716.
- [23] C.M. Oldenburg and F.J. Spera: *Numer. Heat Transf. B*, **21**(1992), 217.
- [24] R. Pardeshi, A.K. Singh and P. Dutta: *Numer. Heat Transf. A*, **55**(2008), 42.
- [25] G.M. Poole and N. El-Kaddah: *J. Iron Steel Res., Intl.*, **19**(Suppl. 1)(2012), 252.
- [26] G.M. Poole and N. El-Kaddah: *Metall. Trans. B*, in press.
- [27] W.P. Jones and B.E. Launder: *Intl. J. Heat Mass Transf.*, **15**(1972), 301.
- [28] D.G. Thomas: *J. Colloid Sci.*, **20**(1965), 267.
- [29] B.E. Launder and D.B. Spalding: *Mathematical Models of Turbulence*, Academic Press, London, (1972), 78.
- [30] W.M. Pun and D.B. Spalding: Report HTS/76/2, Imperial College, London, (1972).
- [31] S.V. Patankar: *Numerical Heat Transfer and Fluid Flow*, Hemisphere Publishing, New York, (1980).

Chapter 5

Numerical Modeling of Macrosegregation in Al-Cu Alloys Solidifying in the Presence of Electromagnetic Stirring

5.1—Abstract

A model for predicting solidification and solute segregation of binary alloys undergoing electromagnetic stirring has been developed in this study. A dual-zone formulation was employed to describe the velocity fields in the bulk liquid and mushy regions. The key feature of this model is that it accounts for the damping of the flow in the suspended particle region via the damping of turbulence at the crystallite surfaces, represented by a damping force given in terms of the turbulent kinetic energy and fraction of solid. Computed macro-segregation results were compared with the experimental measurements. A parametric study that included the effects of current, frequency, dendrite coherency and coil location on segregation was also performed.

5.2—Introduction

Maintaining a uniform distribution of alloying elements is extremely difficult in many casting processes due to solute redistribution during solidification (aka segregation). There are two principal forms of segregation, namely microsegregation and macrosegregation, which occur at different length scales. Microsegregation occurs at the crystallite interfaces due to differences in the phase solubilities of solute, while macrosegregation results from interdendritic convective transport of solute-enriched liquid. Each of these phenomena can lead to significant spatial solute variations and by corollary physical properties.

In recent years, macrosegregation control in electromagnetic (EM) stirring systems has garnered particular interest due to its widespread use in solidification processes to produce

castings exhibiting a fine-grained equiaxed structure [1-5]. Zhang and coworkers [6] found that EM stirring significantly reduced the degree of solute heterogeneity during continuous casting of Al alloy billets. Prescott and Incropera found both experimentally [7] and numerically [8] that intensifying EM stirring reduced overall macrosegregation via increased turbulent mixing. However, other studies, such as those of Budenkova [9] and Griffiths and McCartney [10], found that in certain cases EM stirring can also lead to the formation of regions with positive and negative segregation within the casting.

Recently, there have been substantial efforts to model segregation in EM solidification processes [8,9,11-16]. Doing so requires, above all, an accurate description of the turbulent velocity and electromagnetic field phenomena in the bulk liquid and two-phase “mushy” regions. Generally, modeling the EM field has been accomplished using approximate analytical solutions for the Lorentz force distribution such as those found in References [17,18]. Such solutions, however, can only be found for highly simplified geometries, and thus have minimal flexibility in their application.

The models for the flow in the mushy region may be divided into (i) single-zone [8,12,16,19] and (ii) dual zone models [9,15,20]. Single-zone models treat the flow in the entire mushy region as that of a porous medium governed by Darcy’s law. Such models accurately predict flow behavior for columnar solidification morphologies, but do not account for the presence of floating equiaxed crystallites commonly found in EM solidification systems [21]. Dual-zone models account for this phenomenon by relaxing the porous medium assumption at low fraction solid, treating the flow in this “suspended particle region” as that of a rheological slurry. There have been some efforts to incorporate turbulence into both the single-zone^{8,12} and

dual-zone model formulations [9,15]. However, none of these models have accounted for the crystallite interactions with the turbulent field, which are known to damp the flow [22-24].

Recently, some of the authors [25,26] have proposed an improved dual-zone model formulation for turbulent EM stirred solidification systems. The model solves the EM field equations numerically in both the melt and adjacent conducting domains. The model also accounts for flow damping due to crystallite interactions with the turbulent eddies.

The objective of this work is to examine the applicability of this newly developed theoretical approach to measurements obtained from an experimental EM stirring system. A satisfactory interpretation of these measurements serves a twofold purpose. First, it represents a fundamental test of the model's capabilities; more importantly, however, it allows for an expanded application of the model to more sophisticated systems and operating conditions.

5.3—Model Formulation

The mathematical description for any EM stirred solidification system is given in terms of the momentum and continuity equations for fluid flow, the heat and solute conservations equations for temperature and solute fields, respectively, and the needed subsidiary relationships for the Lorentz forces, Joule heating, and turbulence parameters. Since a substantial number of these equations have been given in previous publications [25,26], the model formulation presented in this work will be that of a broad outline only.

5.3.1—Electromagnetic Field

In two dimensional systems, the mutual inductance method will be used due to its ability to easily solve for the electromagnetic field quantities in the molten metal domain and adjacent conducting media without the need to grid free space. In this method, the conducting region(s) with respective electrical conductivity, σ , are divided into elementary circuits of constant current density, \mathbf{J} . The current density in each circuit is given in terms of the current densities of all of the other circuits by

$$\oint \mathbf{J} \cdot d\mathbf{l}_i = -j\omega\sigma \left[\sum_{m=1}^{metal} M_{i,m} (\mathbf{J} \cdot \mathbf{S})_m + \sum_{c=1}^{shields} M_{i,c} (\mathbf{J} \cdot \mathbf{S})_c + \sum_{k=1}^{coil} M_{i,k} I_k \right] \quad [5-1]$$

where \mathbf{S} and \mathbf{l} are the respective lengths and surface areas of the elementary circuits, j is the square root of -1 , ω is the angular frequency, and $M_{i,j}$ is the mutual inductance given by

$$M_{i,j} = \frac{\mu_0}{4\pi} \iint \frac{d\mathbf{l}_j \cdot d\mathbf{l}_i}{r'} \quad [5-2]$$

From the current density, the magnetic flux density, \mathbf{B} , is given by

$$\mathbf{B} = -\frac{\nabla \times \mathbf{J}}{j\omega\sigma} \quad [5-3]$$

5.3.2—Fluid Flow

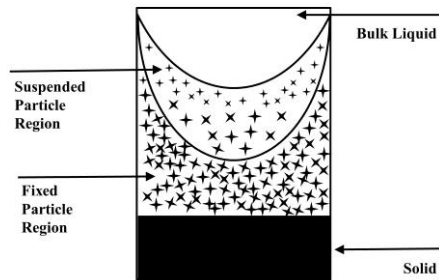


Figure 5.1 Flow domains for the dual-zone solidification model

For the three flow domains shown in Figure 5.1, the continuity momentum conservation equations are respectively given as

$$\nabla \cdot \mathbf{u} = 0 \quad [5-4]$$

$$\rho \frac{\partial \mathbf{u}}{\partial t} + \rho \mathbf{u} \cdot \nabla \mathbf{u} = -\nabla P + \mu \nabla^2 \mathbf{u} + \lambda (\mathbf{J} \times \mathbf{B} + \mathbf{F}_d) - \frac{\mu_t}{K} (\mathbf{u} - \mathbf{u}_s) \quad [5-5]$$

where

$$\mathbf{u} = f_s \mathbf{u}_s + (1 - f_s) \mathbf{u}_l \quad [5-6]$$

and ρ , \mathbf{F}_d , and λ represent the density, turbulent damping force, and a switch parameter, respectively. The quantity $\mathbf{J} \times \mathbf{B}$ is the Lorentz force. In the bulk liquid and suspended particle regions, λ is equal to unity and is zero in the fixed particle region. Since it is assumed that the velocity of solid is equal to velocity of liquid in the bulk liquid and suspended particle region (homogeneous flow model), the Darcy term is finite only in the fixed particle region. The flow permeability, K , was determined using the Carman-Kozeny equation. The turbulent damping force is given by

$$\mathbf{F}_d = \frac{2(1 - f_L^2) \sqrt{c_d} \rho k}{D_g \left(1 - \left(\frac{6(1 - f_L)}{\pi \beta} \right)^{1/3} \right)} \hat{\mathbf{e}}_j \quad [5-7]$$

where β is the sphericity of the crystallites. It should be noted that the coherency fraction solid, f_c , is equal to $6\pi/\beta$ for a simple cubic array of crystallites.

The turbulent characteristics of the flow were given by the low-Re k - ϵ model of Jones and Launder [27], and the effective viscosity, μ , is given as the sum of the laminar and turbulent components, μ_l and μ_t , respectively. It is assumed that turbulence is completely damped in the fixed particle region due to the interparticle spacing in this region being on the same order as the Kolmogorov turbulence length scale [28]. In the bulk liquid and fixed particle regions, the laminar viscosity components are that of the molecular value. In the suspended particle region,

the rheological effect on the laminar viscosity is represented using the correlation developed by Thomas [29].

5.3.3—Heat Transfer

Assuming that the fraction solid, f_s , varies as a piecewise linear function of temperature, T , the differential energy balance equation with phase change is given by

$$\rho C^* \left(\frac{\partial T}{\partial t} + \mathbf{v} \cdot \nabla T \right) = \nabla \cdot (k^* \nabla T) + \frac{\|\mathbf{J}\|^2}{\sigma} \quad [5-8]$$

where the last term accounts for electrical energy dissipation (aka Joule heating). The quantity C^* is the effective specific heat given in terms of the molecular specific heats of each phase, $c_{p,i}$, the latent heat L , and the solidus and liquidus temperatures T_s and T_L , respectively, by

$$C^* = \begin{cases} c_{p,l} & T \geq T_L \\ c_{p,s} + \frac{L}{T_i - T_j} & T_s < T < T_L \\ c_{p,s} & T \leq T_s \end{cases} \quad [5-9]$$

The quantities T_i and T_j represent the end point temperatures of a line segment of the f_s vs T curve. The effective thermal conductivity, k^* , is given by

$$k^* = \begin{cases} k_l + \frac{\mu_l c_{p,l}}{\text{Pr}} & T \geq T_L \\ (1 - f_s) k_l + f_s k_s & T_s \leq T < T_L \\ k_s & T \leq T_s \end{cases} \quad [5-10]$$

In the bulk liquid, the effective thermal conductivity is given by the sum of the turbulent and molecular contributions, where Pr is the turbulent Prandtl number.

5.3.4—Solute Segregation

For a binary alloy, the overall mass conservation equation for the solute species in a two-phase system is given by:

$$\begin{aligned} \frac{\partial}{\partial t}(\rho_s g_s C_s + \rho_l g_l C_l) + \nabla \cdot (\rho_s g_s \mathbf{v}_s C_s + \rho_l g_l \mathbf{v}_l C_l) \\ = \nabla \cdot (\rho_s g_s D_s \nabla C_s + \rho_l g_l D_l \nabla C_l) \end{aligned} \quad [5-11]$$

The mass fraction solid, f_i , and the volume fraction solid, g_i , of a any particular phase are related by

$$f_i = \frac{\rho_i g_i}{\rho} \quad [5-12]$$

Using Equation (5-12), along with the assumptions made by Chang and Stefanescu [30], Equation (5-11) can be generally rewritten as

$$\rho f_L \frac{\partial C_L}{\partial t} + \rho f_L \mathbf{v}_L \cdot \nabla C_L = \nabla \cdot (\rho f_L D_L \nabla C_L) + \Omega \quad [5-13]$$

where Ω is the solute rejection source term given by

$$\Omega = \begin{cases} \rho(1-k_0)C_L \left(\frac{\partial f_s}{\partial t} + \mathbf{v}_s \cdot \nabla f_s \right) & 0 < f_s \leq f_c \\ \rho(1-k_0)C_L \frac{\partial f_s}{\partial t} & f_c < f_s \leq 1 \end{cases} \quad [5-14]$$

where k_0 is the equilibrium partition coefficient. Like the thermal conductivity, the mass diffusivity is given as the sum of the molecular and laminar contributions:

$$D_L = D_m + \frac{\mu_t / \rho}{Sc} \quad [5-15]$$

where D_m is the molecular value of the liquid diffusivity, and Sc is the turbulent Schmidt number, generally taken to be approximately unity [31].

5.4—Results and Discussion

In this section, we will present the computed results for Al-4.5%Cu alloy under unidirectional solidification in a bottom chill mold surrounded by an induction coil, along with a comparison with measured segregation profiles. The thermophysical properties used in the analysis are given in Table 5.1. The calculations were performed on a 40x25 grid for the coil current and frequency used in a previous experiment [32], with the dimensions of the system given in Figure 5.2 The calculations used a characteristic grain size of 200 μm and a coherency fraction solid of 0.2 ($\beta=0.3821$), which is characteristic of highly aspherical crystallites.

| | |
|-----------------------------|--------------------------------------|
| Solid Density | 2800 kg/m ³ |
| Liquid Density | 2300 kg/m ³ |
| Solid thermal conductivity | 100 W/m-°C |
| Liquid thermal conductivity | 100 W/m-°C |
| Solid heat capacity | 1070 J/kg-°C |
| Liquid heat capacity | 1070 J/kg-°C |
| Liquid mass diffusivity | 3*10 ⁻⁹ m ² /s |
| Electrical Conductivity | 1.28*10 ⁶ Mho/m |
| Liquidus temperature | 648°C |
| Solidus temperature | 564°C |
| Latent heat of fusion | 389000 J/kg |
| Molecular viscosity | 1.5*10 ⁻³ Pa-s |
| Initial temperature | 675°C |
| Heat transfer coefficient | 250 W/m ² -°C |
| Grain geometry factor | 0.3821 |
| Characteristic grain size | 200 μm |

Table 5.1. Thermophysical properties used in the present study

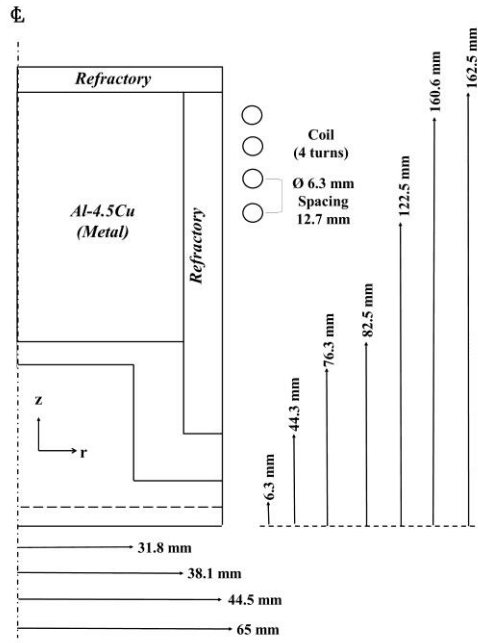


Figure 5.2 Dimensions of the system used in this study

5.4.1—Computed Results

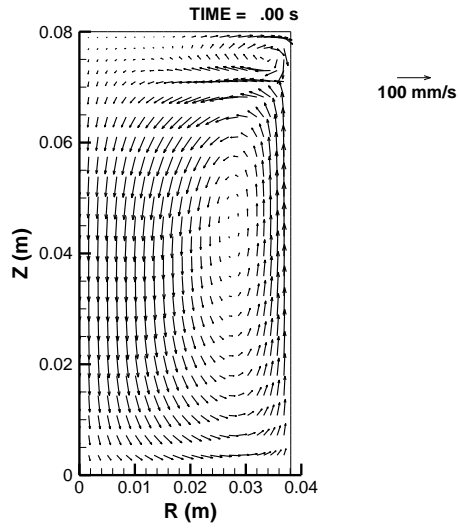


Figure 5.3. Initial computed velocity field

Figure 5.3 shows the computed initial velocity field in the melt. As seen in this figure, the flow consists of one primary, counterclockwise recirculating loop, accompanied by a secondary, clockwise flow loop near the free surface of the melt. It should be noted that this flow is similar to those found by the authors in Reference [26].

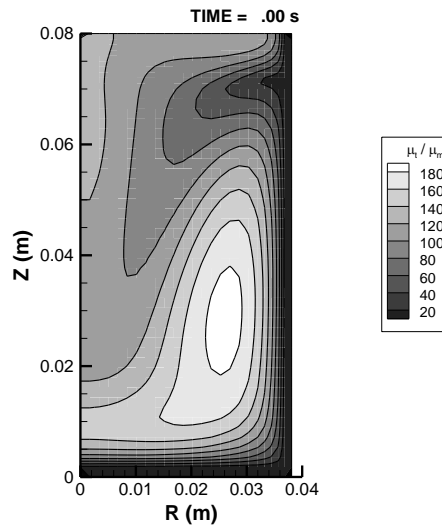


Figure 5.4. Initial turbulent field given in terms of turbulent to molecular viscosity

Figure 5.4 shows the computed initial turbulent field. Note that the turbulent field is presented in terms of the ratio between the turbulent and laminar viscosities ($\mu^* = \mu_t / \mu_l$). As expected, turbulence is strongest near the vortex center of the primary flow loop at approximately 190 times the molecular viscosity, where the shear strain rate is highest. This result suggests that there will be significant turbulent mixing in this region of the melt, leading to homogenization of both the temperature and solute fields during solidification.

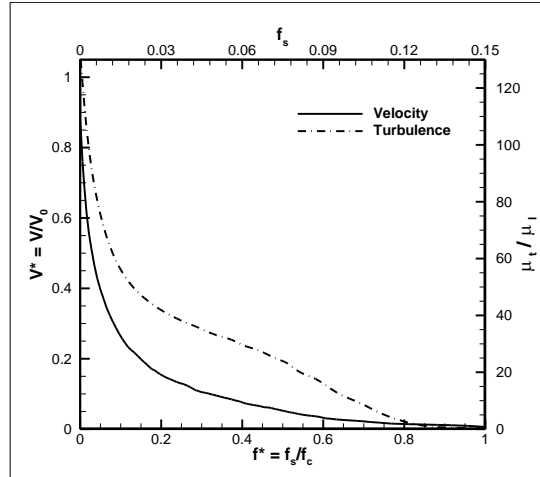


Figure 5.5 Damping of the velocity and turbulent fields. Data taken at the centerline 20mm from the chill.

As solidification progresses, there is significant damping of the flow in the mushy region due to the interaction of the turbulent eddies with the crystallites. This is clearly illustrated in Figure 5.5, which show the variation of the velocity and turbulent fields with respect to solid fraction. The values presented for the velocity have been normalized with the value at zero fraction solid and the solid fraction is shown in both normalized and actual values. The velocity decreases rapidly in the initial stages of solidification ($f_s < 0.05$) due to the high values of turbulence; it then levels off at around 10 pct of its initial value near fraction solid of 0.03. The reason for this plateau is shown by the change in turbulent viscosity, where the decreased turbulent kinetic energy of the flow leads to smaller increases in the damping forces per unit of solid fraction.

Figures 5.6 and 5.7 show the liquid solute concentration profile at times of 360s and 400s, respectively. After 360s, Figure 5.6, the liquid concentration starts at ranges from 5.1-6% Cu. and the the solute concentration monotonically decreases with height at the outer radius. The concentration is more or less homogeneous in the interior of the ingot, and the solutal isolines

tend to align themselves with the flow direction, indicating that convection is dominant with regards to mass transport. At 550s, Figure 5.6, there are still two recirculating loops in the melt, but the secondary loop has shifted inward and has grown in size at the expense of the primary recirculating loop. Furthermore, the turbulent damping of the flow by the crystallites has led to a change in the solute profile, as the isolines have begun to align themselves normal to the direction of heat extraction due to the decrease in convective intensity. This suggests that the final axial segregation profiles for any given radial value will be markedly different from one another.

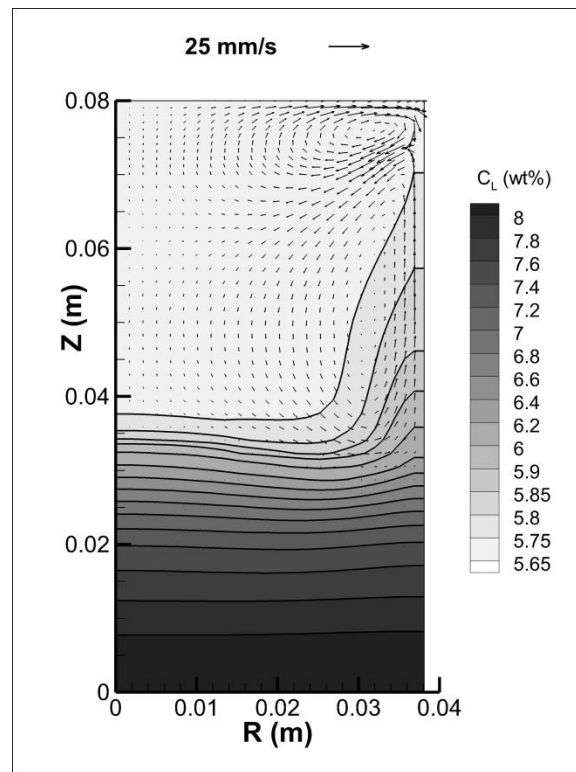


Figure 5.6 Computed velocity and liquid solute profile after 360s for frequency of 4900 Hz.

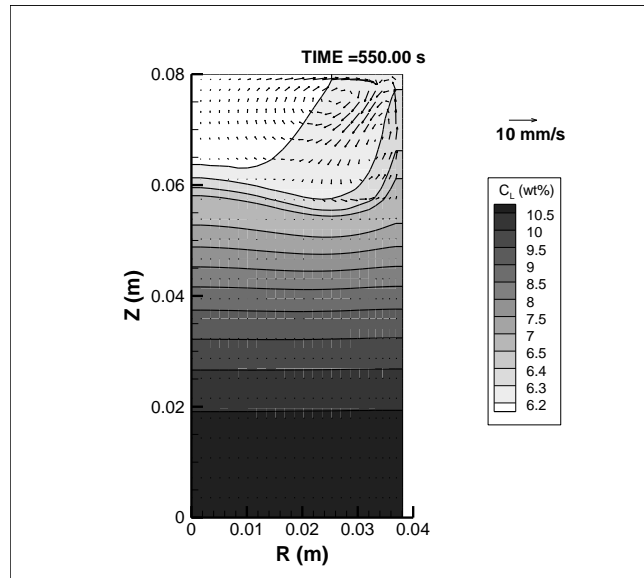


Figure 5.7. Solute segregation profile after 550s. Note the change of scale in the velocity.

The evolution of the computed axial concentration profiles, taken at the centerline for various times during solidification, is shown in Figure 5.8. It is clearly seen that the concentration starts at the initial value, C_0 , of 4.5% Cu. As solidification progresses, the washing of solute from the fixed particle region to the suspended particle region via convection causes the curves to undergo an inflection near the middle of the axis height, causing the top of the ingot to reach eutectic composition first. This may be contrasted with the work of Chang and Stefanescu [30] on solidification of Al-Cu alloy without forced convection, where there was a significant amount of inverse segregation present. It should also be noted that those which assume an equilibrium solid composition [8,33,34] only attain a maximum composition of $C_0/k_0 = 26.16$ wt% Cu, meaning that there should be no eutectic at the conclusion of solidification. As shown in the scanning electron micrograph and Cu composition map in Figure 5.9, this is clearly not the case. It can be easily seen in this figure that there is a significant amount of eutectic outlining the dendrites.

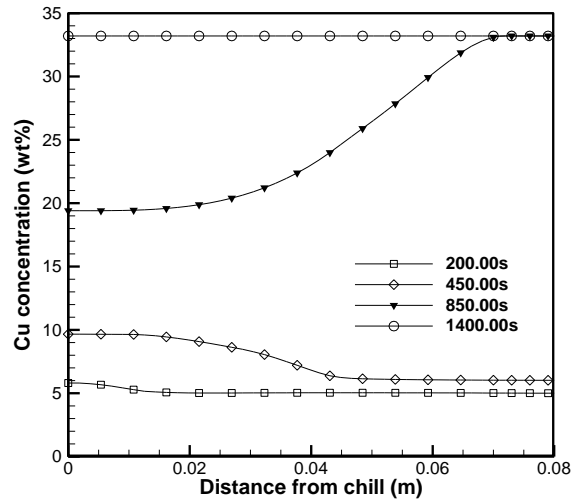
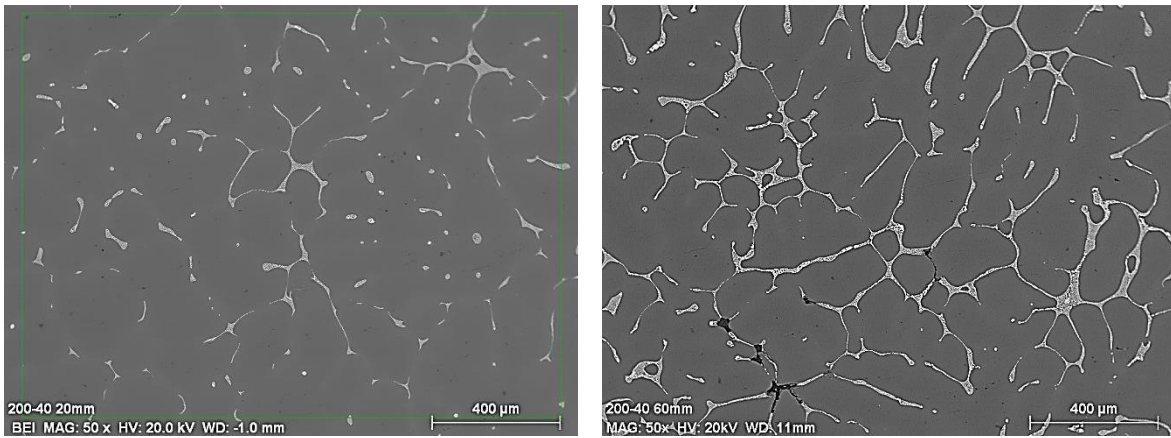


Figure 5.8. Axial liquid concentration profiles, taken at the centerline for different stages of solidification.



(a)

(b)

Figure 5.9 Electron backscatter micrographs taken for EM stirred sample at (a) 20mm and (b) 60mm from chill block. Images taken at ingot centerline.

5.4.2—Comparison with Experimental Measurements

The model was finally validated by comparing the final computed compositional profiles with measured data. As seen in Figure 5.10, there is good agreement between the predicted results and the measured stirred and unstirred solute profiles. It is also seen that stirring using a

stationary magnetic field results in increased segregation along the ingot height. This is again consistent with the micrographs in Figure 5.9, where the washing of solute from the fixed particle region to the suspended particle region has led to a higher eutectic fraction at 60mm from the chill, Figure 5.9b, compared with that at 20mm, Figure 5.9a. While this is not advantageous in ensuring homogeneous castings, these results suggest that stirring under these conditions may be useful in solidification processes where it is desirable to remove unwanted solute.

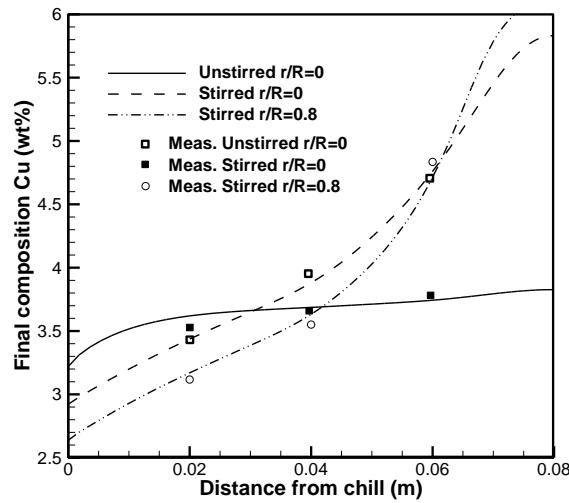


Figure 5.10 Final computed composition profiles at different radii compared with experimental measurements.

5.4.3—Influence of Various Parameters

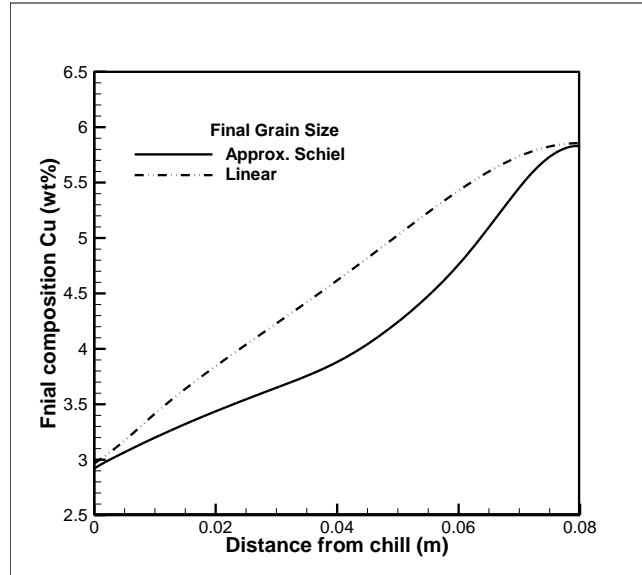


Figure 5.11. Influence of assumed f_s vs T profile on the final solute composition at the centerline.

It is also instructive to examine the influence of various model inputs on the final composition profile. Figure 5.11 shows the final centerline composition curves for two different fraction solid versus temperature profiles. As seen in this figure, the computed compositions at the chill base and the free surface are the same when linear evolution of fraction solid. However, assuming a linear f_s vs T profile for heat transfer while using the Scheil assumptions for mass transfer, which has been done in other works [30], leads to an overestimation of final composition compared to the piecewise Scheil curve; this is due to the increased solute rejection from the solid into the liquid. This result illustrates the importance of coupling the fraction solid evolution assumptions between the temperature and solute conservation equations, as failure to do so will lead to spurious model results.

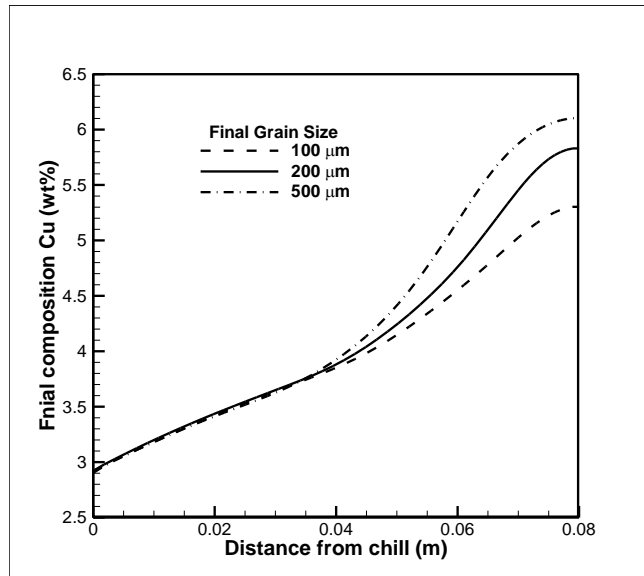


Figure 5.12 Influence of final grain size on the final centerline composition

Figure 5.12 shows the influence of final grain size on the final solute profile in the cast alloy. As seen in this figure, the amount of centerline segregation increases in the upper half of the casting for increasing grain size. As explained in the authors' previous work [25], the increase in particle size reduces the specific surface area under which turbulent damping can occur, leading to increased flow intensity and increased washing effect of solute from other parts of the casting as well. The results shown here are also consistent with those in Figure 5.10, where the intensity of segregation decreases as the velocity of the flow tends to zero in the case of the unstirred melt, and is also consistent with previous experiments [35,36], which showed that there is decreased segregation in castings exhibiting highly refined grain structures.

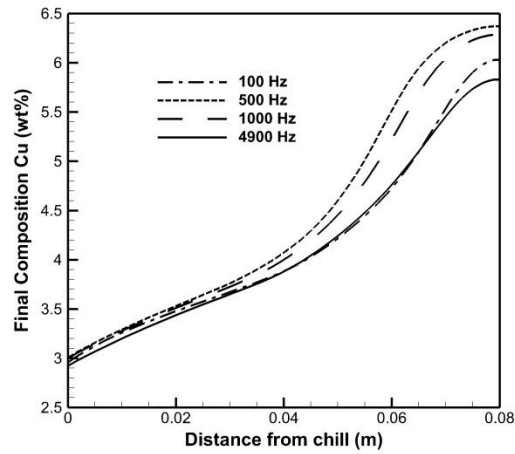


Figure 5.13 Effect of frequency of centerline segregation

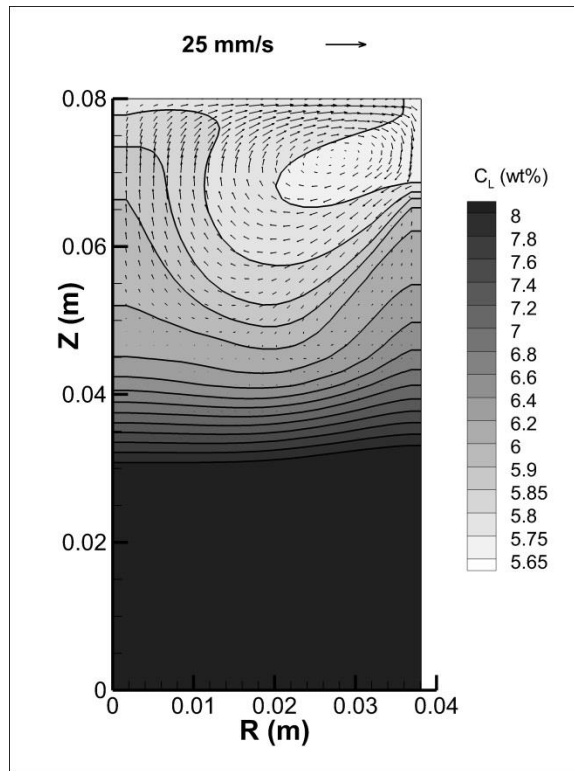


Figure 5.14 Velocity and liquid solute concentration field after 360 seconds for a frequency of 500Hz

The frequency also has a profound effect on centerline segregation. Figure 5.13 shows the variation of solute concentration along the centerline for four different frequencies. As frequency decreases, segregation in the upper half of the ingot becomes more severe until the

frequency is 100 Hz, after which composition becomes more uniform. This is best explained by examining Figure 5.14, which shows the liquid composition profile after 360s for a coil frequency of 500 Hz. It is seen that the decrease in frequency has led to an expansion of the upper recirculating loop in size such that it approximately covers the upper half of the ingot, while the flow in the lower recirculating loop has been damped significantly. Whereas the dominant, counterclockwise flow recirculation at 4900 Hz caused rejected solute to be primarily taken up at the outer radius, Figure 5.6, the reversal of the flow direction in the upper loop, Figure 5.14, causes a solute buildup at the centerline for the upper half of the ingot, leading to greater incorporation of alloying elements into the solid phase. It should be noted, however, that decreasing the operating frequency causes a likewise decrease in the magnitude of the Lorentz forces in the melt. This counteracts the recirculation loop expansion effect and lessens segregation. Due to these opposing effects, these results suggest that it may be more suitable to use travelling magnetic fields when performing EM stirring at elevated frequencies to eliminate the upper recirculating loop or to use magnetic shields along with the stationary field to alter the flow structure [37].

5.5—Conclusions

A model for predicting solidification and solute segregation of binary alloys undergoing electromagnetic stirring has been presented. A dual-zone formulation was employed to describe the velocity fields in the bulk liquid and mushy regions. The key feature of this model is that it accounts for the damping of the flow in the suspended particle region via the damping of turbulence at the crystallite surfaces, represented by a damping force given in terms of the turbulent kinetic energy and fraction of solid. The formulation for computing the solute field utilized a no solid diffusion assumption at the microscopic level. Computed results for the

solidification of Al-4.5%Cu alloy showed that segregation is nearest the chill at the beginning of solidification, with washing of solute by the flow in the suspended particle region causing an inflection point to be reached as solidification progresses. The computed results were also compared, and found to be in good agreement, with experimental measurements. Therefore, it may be generally said that this model offers a rigorous mathematical framework for describing the flow behavior and solute segregation in electromagnetically stirred melts, and may be applied as a design tool to predict the behavior of other EM solidification processes.

5.6—References

- [1] T Campanella, C Charbon, M Rappaz: ‘Influence of permeability on the grain refinement induced by forced convection in copper-base alloys’, *Scripta Mater.*, 2003, **49**, 1029-1034.
- [2] M Paes, EG Santos, EJ Zoqui: ‘Obtention rheocast microstructure for Al-4.5wt%Cu alloy: Comparison ultra-refining and electromagnetic stirring’, *J. Achievements in Mater. and Manufact. Eng.*, 2006, **19**, 21-28.
- [3] AN Turchin, DG Eskin, L Katgerman: ‘Effect of melt flow on macro- and microstructure evolution during solidification under forced flow conditions’, *Mater. Sci. Eng. A*, 2005, **413-414**, 98-104.
- [4] N Barman, P Dutta: ‘Evolution of microstructure during solidification of an aluminum alloy under stirring’, *Trans Indian Inst Metals*, 2012, **65**, 683-687.
- [5] E Jiang, E Wang, G Zhan, A Deng, J He: ‘Effect of rotating electromagnetic stirring on solidification structure of Incoloy 800H’, *Proc. of 7th Intl. Conf. on ‘Electromagnetic Processing of Materials’*, Beijing, China, October 2012, 313-316.
- [6] B Zhang, J Cui, G Lu: ‘Effects of low-frequency electromagnetic field on microstructures and macrosegregation of continuous casting of 7075 aluminum alloy’, *Materials Science and Engineering A*, 2003, **355**, 325-330.
- [7] PJ Prescott, FP Incropera, DR Gaskell. Influence of electromagnetic stirring on the solidification of a binary metal alloy. *Experimental Heat Transfer A*, 1996, **9**, 105-131.
- [8] PJ Prescott, FP Incropera. ‘The effect of turbulence on solidification of a binary metal alloy with electromagnetic stirring’, *J. Heat Transf.*, 1995, **117**, 716-724.

- [9] O. Budenkova, F. Baltaretu, J. Kovács, A. Roósz, A. Rónaföldi, A.M. Bianchi, and Y. Fautrelle: ‘Simulation of a directional solidification of a binary Al-7wt%Si and a ternary alloy Al-7wt%Si-1wt%Fe under the action of a rotating magnetic field’, IOP Conf. Ser.: Mater. Sci. Eng., 2012, **33**, 012046.
- [10] W. Griffiths and D. McCartney: ‘The effect of electromagnetic stirring during solidification on the structure of Al-Si alloys’, Mater. Sci. Eng. A, 1996, **216**, 47-60.
- [11] P.J. Prescott and F.P. Incropera: ‘Magnetically damped convection during solidification of a binary metal alloy’, J. Heat Transf., 1993, **115**, 302-310.
- [12] W. Shyy, Y. Pang, G. Hunter, D.Y. Wei, and M.H. Chen: Intl. J. Heat Mass Transf., 1992, vol. 35, 1229-1245.
- [13] J. Partinen, N. Saluja, J. Szekely, and J. Kirtley: ‘Experimental and computational investigation of rotary electromagnetic stirring in a woods metal system’, ISIJ Intl, 1994, **9**, 707-714.
- [14] R. Lantzsch, V Galindo, I. Grants, C. Zhang, O. Paetzold, G. Gerbeth, and M. Stelter: ‘Experimental and numerical results on the fluid flow driven by a traveling magnetic field’, J. Crystal Growth, 2007, **305**, 249-256.
- [15] R. Pardeshi, A.K. Singh, and P. Dutta: ‘Modeling of solidification process in a rotary electromagnetic stirrer’, Numer. Heat Transfer A, 2008, **55**, 42-57.
- [16] S. Simlandi, N. Barman, H. Chattopadhyay: ‘Studies on Transport Phenomena during Continuous Casting of an Al-Alloy in Presence of Electromagnetic Stirring’, Trans. Indian Inst. Met., 2013, **66**, 141-146.
- [17] K.H. Spitzer, M. Dubke, and K. Schwerdtfeger: Metall. Trans. B, 1986, **17**, 119.
- [18] S. Milind and V. Ramanarayanan: IEEE-IAS Conf., 2004, pp. 188-194.
- [19] R. Mehrabian, M. Keane and M.C. Flemings: ‘Interdendritic fluid flow and macrosegregation; influence of gravity’, Metall. Trans., 1970, **1**, 455-464.
- [20] C.M. Oldenburg and F.J. Spera: ‘Hybrid model for solidification and convection’, Numer. Heat Transf. B, 1992, **21**, 217-229.
- [21] C.J. Parides, R.N. Smith, and M.E. Glicksman: ‘The influence of convection during solidification on fragmentation of the mushy zone of a model alloy’, Metall. Trans. A, 1997, **28**, 875-883.
- [22] Y. Yamagishi, H. Takeuchi, A.T. Pyatenko, and N. Kayukawa: ‘Characteristics of microencapsulated PCM slurry as a heat-transfer fluid’, AIChE J., 1999, **45**, 696-707.

- [23] J.L. Alvarado, C. Marsh, C. Sohn, G. Phetteplace, and T. Newell: ‘Thermal performance of microencapsulated phase change material slurry in turbulent flow under constant heat flux’, *Intl. J. Heat Mass Transf.*, 2007, **50**, 1938-1952.
- [24] S. Wenji, X. Rui, H. Chong, H. Shihui, D. Kaijun, and F. Ziping: ‘Experimental investigation on TBAB clathrate hydrate slurry flows in a horizontal tube: Forced convective heat transfer behaviors’, *Intl. J. Refrig.*, 2009, **32**, 1801-1807.
- [25] G.M. Poole and N. El-Kaddah: ‘An improved model for the flow in an electromagnetically stirred melt during solidification’, *Metall. Trans. B*, 2013, **44**, 1531-1540.
- [26] G.M. Poole and N. El-Kaddah: ‘The effect of coil design on the temperature and velocity fields during solidification in electromagnetic stirring processes’, *ISIJ Intl.*, 2014, **54**, 321-327.
- [27] W.P. Jones and B.E. Launder: ‘The prediction of laminarization with a two-equation model of turbulence’, *Intl. J. Heat Mass Transf.*, 1972, **15**, 301-314.
- [28] H. Tennekes and J.L. Lumley: ‘A first course in turbulence’, 19-20; 1972, Cambridge, MIT Press.
- [29] D.G. Thomas: Transport characteristics of suspensions; VIII. A note on the viscosity of Newtonian suspensions of uniform spherical particles’, *J. Colloid Sci.*, 1965, **20**, 267-277.
- [30] S. Chang and D.M. Stefanescu: ‘A model for macrosegregation and its applications to Al-Cu castings’, *Metall. Trans. A*, 1996, **27**, 2708-2721.
- [31] J. Szekely and N. El-Kaddah: ‘Turbulent recirculating flows in metals processing’, *Proc. of Intl. Sem. on ‘Refining and alloying of liquid aluminum and ferro-alloys’*, Trondheim, Norway, August 1985, 249-266.
- [32] M.J. Heyen: ‘Effect of electromagnetic stirring on grain refinement of Al-4.5% Cu alloy’, MS Thesis, University of Alabama, Tuscaloosa, AL, USA, 21-40
- [33] J. Chowdhury, S. Ganguly, and S. Chakraborty: ‘Numerical simulation of transport phenomena in electromagnetically stirred semi-solid materials processing’, *J. Phys. D: Appl. Phys.*, 2005, **38**, 2869-2880.
- [34] K.C. Chiang and H.L. Tsai: ‘Shrinkage-induced fluid flow and domain change in two-dimensional alloy solidification’, *Intl. J. Heat Mass Transf.*, 1992, **35**, 1763-1770.
- [35] G. Poole, N. Rimkus, A. Murphy, P. Boehmcke, and N. El-Kaddah: ‘Effect of the solidification rate on microstructure of cast Mg alloys at low superheat’, in *Proc. of ‘Magnesium Technology 2012’*, Orlando, USA, March 2012, 161-164.

- [36] Y. He, A. Javaid, E. Essadiqi, and M. Shehata, 'Numerical Simulation and Experimental Study of the Solidification of a Wedge-Shaped AZ31 Mg Alloy Casting', *Canadian Metall Quart.*, 2009, **48**, 145-156.
- [37] J.L. Meyer, N. El-Kaddah, J. Szekely, C. Vives, and R. Ricou. 'A comprehensive study of the induced current, the electromagnetic force field, and the velocity field in a complex electromagnetically driven flow system', 1987, **18**, 529-538.

Chapter 6

Conclusions and Future Work

6.1—Concluding Remarks

1. A mathematical model has presented which describes the electromagnetic, fluid flow, heat transfer, and solute segregation phenomena in the bulk liquid, mushy, and solid region for EM stirred solidification systems.
2. A dual-zone flow model was used to describe fluid flow in the mushy region by dividing the domain into the fixed particle and suspended particle regions, with the boundary being defined by the coherency fraction solid.
3. Damping of the flow in the suspended particle region occurs through interaction of the turbulent stresses with the crystallite surfaces, and an expression was developed for describing the turbulent damping force in terms of the turbulent kinetic energy, fraction solid, and the geometry of the crystallites.
4. Calculations were carried out for solidification of Al-Cu alloy in a bottom chill mold for various coil frequencies and positions.
5. It was found that the velocity damping takes place in the initial stages of solidification ($f_s < 0.1$), and the velocity in the suspended particle region was an order of magnitude smaller than that of the bulk liquid. Full laminarization occurs around f_s equal to 0.3.
6. The strength of the damping force was lessened with both larger grain size and small values of coherency solid fraction.
7. Neglecting the damping force leads to a gross overestimation of the flow intensity and turbulent characteristics of the flow in the mushy region.

8. Darcian behavior in the fixed particle region further reduced the velocity, with the fluid reaching negligible values a few millimeters below the coherency isotherm. The penetration depth of the flow was shown to increase with lower coherency values.
9. The coil position was shown to have a substantial difference on the flow structure in the bulk liquid, which in turn affected the local solidification profiles in the mushy region.
10. The flow and turbulent decay rates with respect to fraction solid were found to be independent of coil position.
11. Although the overall solidification rate was unchanged by the coherency value or final grain size, there were local effects of the flow with respect to the suspended particle region. The cooling rate in the initial stages of solidification was shown to increase for larger grain size.
12. The computed model results for solute segregation was compared with experiments, and the model results were found to be in good agreement with measurements.
13. It was found that using different evolutionary behaviors for latent heat release and solute transfer formulation led to large deviations from measurements

6.2—Recommendations for Future Research

1. Investigate the effect of placing conducting materials in proximity to the coil on the flow structure and intensity, along with the subsequent effects on the temperature evolution and solute segregation within the cast alloy
2. Further evaluate the model using benchmark problems from literature to identify potential pitfalls in the model and make adjustments.
3. Implement a deterministic formulation for latent heat release and solute rejection while incorporating into the flow the resulting microstructural characteristics of the crystallites.

References

- [1] AA Tzavaras, HD Brody: Electromagnetic stirring and continuous casting: Achievements, problems, and goals. *JOM*, 36(3)(1984), 31-37.
- [2] BA Sivak, VG Grachev, VM Parshin, AD Chertov, SV Zarubin, VG Fisenko, AA Solov'ev: MHD processes in the electromagnetic stirring of liquid metal in continuous section and bloom casters. *Metallurgist (Russian)*, 53(2009), 469-481.
- [3] JL Meyer, J Szekely, N El-Kaddah, C Vives, R Ricou: Electromagnetic and fluid flow phenomena in a mercury model system of the electromagnetic casting of aluminum. *Metall. Trans. B*, 18(1987), 539-548.
- [4] Z Zhao, J Cui, J Dong, B Zhang: Effect of low-frequency magnetic field on microstructures and macrosegregation of horizontal direct chill casting 7075 aluminum alloy. *J. Mater. Process. Tech.*, 182(2007), 185-190
- [5] QF Zhu, ZH Zhao, JZ Cui, YB Zuo, XJ Wang: Effect of combined application of electromagnetic fields on horizontal direct chill casting of 7050 aluminium alloy. *Mater. Sci. Tech.*, 24(2008), 560-566.
- [6] G Poole, N Rikus, A Murphy, P Boehmcke, N El-Kaddah: Effect of the solidification rate on microstructure of cast Mg alloys at low superheat. in *Magnesium Technology 2012*. eds. SN Mathaudhu, WH Sillekens, NR Neelameggham, N Hort (Warrendale: TMS, 2012), 161-164.
- [7] C Mahato, M Shamsuzzoha, N El-Kaddah: Solidification Morphology and Structure of Cast Al-Li 2090 Alloy at Low Superheats. in *Solidification of Aluminum Alloys*. eds. MG Chu, DA Granger, Q Han (TMS, Warrendale, OH, 2004) , 321-328.
- [8] X Wang, N Ma: Semiconductor crystal growth by the vertical Bridgman process with transverse rotating magnetic fields. *J. Heat Transf.*, 129(2005), 241-243.
- [9] X Wang, N Ma, DF Bliss, GW Iseler, P Becla: Combining static and rotating magnetic fields during modified vertical Bridgman crystal growth. *J Thermophys. Heat Transf.*, 21(2007), 736-743.
- [10] C Vives, C Perry. Effect of electromagnetic stirring during the controlled solidification of tin. *Intl. J. Heat Mass Transf.*, 29(1986), 21-33.
- [11] L Hachani, B Saadi, XD Wang, A Nouri, K Zaidat. Experimental analysis of the solidification of Sn-3wt%Pb alloy under natural convection. *Intl. J. Heat Mass Transf.*, 55(2012), 1986-1996.
- [12] SF Liu, LY Liu, LG Kang. Refinement role of electromagnetic stirring and strontium in AZ91 magnesium alloy. *J. Alloys Compounds*, 450(2008) 546-550.

- [13] Q Han, A Hellawell. Primary particle melting rates and equiaxed grain nucleation. *Met. Mater. Trans. B*, 28(1997), 169-173.
- [14] B Chalmers. *Principles of Solidification*. (New York: Wiley, 1964).
- [15] Q Zhao, XG Zhang, CF Fang, N Zhang, YB Han, JS Guo, XG Huo. The effects of electromagnetic stirring on the solidification structure and macrosegregation of Pb-Sn alloy. *Adv. Mater. Res.* 484(2012), 1447-1452.
- [16] B Wang, Y Yang, W Tang. Microstructure refinement of AZ91D alloy solidified with pulsed magnetic field. *Trans. Nonferrous Met. Soc. China* 18(2008), 536-540.
- [17] B Willers, S Eckert, U Michel, I Haase, G Zouhar. The columnar-to-equiaxed transition in Pb-Sn alloys affected by electromagnetically driven convection. *Mat. Sci. Eng. A* 402(2005), 55-65.
- [18] KA Jackson, JD Hunt, DR Uhlmann, TP Seward III. On the origin of the equiaxed zone in castings. *Trans. Met. Soc. AIME*, 236 (1966), 149-158.
- [19] CJ Parides, RN Smith, ME Glicksman. The influence of convection during solidification on fragmentation of the mushy zone of a model alloy. *Met. Trans. A* 28(1997), 875-883.
- [20] B Li, HD Brody, A Kazimirov. Real-time observation of dendrite coarsening in Sn-13wt%Bi alloys by synchrotron microradiography. *Phys. Rev. E* 70(2004), 062602.
- [21] D Ruvalcaba, RH Mathiesen, DG Eskin, L Arnberg, L Katgerman. In-situ observation of dendrite fragmentation due to local solute-enrichment during directional solidification of an aluminum alloy. *Acta. Mater.* 55(2007), 4287-4292.
- [22] N El-Kaddah, J Szekely. The turbulent recirculating flow in a coreless induction furnace, a comparison of theoretical predictions with measurements. *J. Fluid Mechanics* 133(1983), 33-46.
- [23] WD Griffiths, DG McCartney. The effect of electromagnetic stirring during solidification on the structure of Al-Si alloys. *Mater. Sci. Eng. A* 216(1996), 47-56.
- [24] V Travnikov, PA Nikrityuk, K Eckert, D Rabinger, S Odenbach, S Eckert. Radial solidification of Al-Si alloys in the presence of a rotating magnetic field. *IOP Conf. Ser.: Mater. Sci. Eng.*, 33(2012), 012048.
- [25] JA Burton, RC Prim, WP Schlichter. The distribution of solute in crystals grown from the melt—Part I: Theoretical. *J. Chem. Phys.* 21(1953), 1987-1991.
- [26] ED Tarapore, JW Evans. Fluid velocities in induction melting furnaces: Part I. Theory and laboratory experiments *Metall. Trans. B*, 7(1976), 343-351.
- [27] ED Tarapore, JW Evans, J Langfeldt. Fluid velocities in induction melting furnaces: Part II. large scale measurements and predictions. *Metall. Trans. B*, 8(1977), 179-184.

- [28] K. Nakanishi, T. Fujii and J. Szekely. Possible relationship between energy dissipation and agitation in steel-processing operations. *Ironmak. Steelmak.*, **2**(1975), 193.
- [29] N. El-Kaddah, J. Szekely, E. Taberlet and Y. Fautrelle. Turbulent recirculating flow in induction furnaces: A comparison of measurements with predictions over a range of operating conditions. *Metall. Trans. B*, **17**(1986), 687.
- [30] N. El-Kaddah, J. Szekely and G. Carlsson. Fluid flow and mass transfer in an inductively stirred four-ton melt of molten steel: A comparison of measurements and predictions *Metall. Trans. B*, **15**(1984), 633.
- [31] SD Ridder, S Kou, R Mehrabian. Effect of fluid flow on macrosegregation in axisymmetric ingots. *Met. Trans. B* 12(1981), 435-447.
- [32] VR Voller, C Prakash. A fixed grid numerical modeling methodology for convection-diffusion mushy region phase-change problems. *Int. J. Heat Mass Transfer* 30(1987), 1709-1719.
- [33] WD Bennon, FP Incropera. A continuum model for momentum, heat, and species transport in binary solid-liquid phase change systems—I: Model formulation. *Int. J. Heat Mass Transfer* 30(1987), 2161-2170.
- [34] T Campanella, C Charbon, M Rappaz. Influence of permeability on the grain refinement induced by forced convection in copper-base alloys. *Scripta Mater.* 49(2003), 1029-1034.
- [35] PC Carman. Fluid flow through granular beds. *Trans. Inst. Chem. Eng.* 15(1937), 150-166.
- [36] DR Poirier. Permeability for flow of interdendritic liquid in columnar-dendritic alloys. *Met. Trans. B* 18(1987), 245-255.
- [37] W Shyy, Y Pang, GB Hunter, DY Wei, MH Chen. Modeling of turbulent transport and solidification during continuous ingot casting. *Int. J. Heat Mass Transfer* 35(1992), 1229-1245.
- [38] PJ Prescott, FP Incropera. The effect of turbulence on solidification of a binary metal alloy with electromagnetic stirring. *J. Heat Transfer* 117(1995), 716-724.
- [39] CM Oldenburg, FJ Spera. Hybrid model for solidification and convection. *Num. Heat Transfer B* 21(1992), 217-229.
- [40] CY Wang, S Ahuja, C Beckermann, HC de Groh III. Multiparticle interfacial drag in equiaxed solidification. *Met. Trans. B* 26(1995), 111-119.
- [41] PA Nikrityuk, K Eckert, R Grundmann. A numerical study of unidirectional solidification of a binary metal alloy under influence of a rotating magnetic field. *Int J Heat Mass Transfer* 49(2006), 1501-1515.

- [42] R Pardeshi, AK Singh, P Dutta. Modeling of solidification process in a rotary electromagnetic stirrer. *Num Heat Transfer A* 55(2008), 42-57.
- [43] GM Poole: Modeling of electromagnetic, heat transfer, and fluid flow phenomena in an EM stirred melt during solidification. MS Thesis, University of Alabama, 2012.
- [44] G.M. Poole and N. El-Kaddah: ‘An improved model for the flow in an electromagnetically stirred melt during solidification’, *Metall. Trans. B*, 2013, **44**, 1531-1540.
- [45] G.M. Poole and N. El-Kaddah: ‘The effect of coil design on the temperature and velocity fields during solidification in electromagnetic stirring processes’, *ISIJ Intl.*, 2014, **54**, 321-327.
- [46] C Stelian, Y Delannoy, Y Fautrelle, T Duffar. Solute segregation in directional solidification of GaInSb concentrated alloys under alternating magnetic fields. *J. Crystal Growth*, 266(2004), 207-215.
- [47] N Barman, P Dutta. Effect of process parameters on transport phenomena during solidification in the presence of electromagnetic stirring. *Trans. Indian Inst. Metals*, 62(2009), 469-474.
- [48] KH Spitzer, G Reiter, K Schwerdtfeger. Multi-frequency electromagnetic stirring of liquid metals. *ISIJ Intl.*, 36(1996), 487-492.
- [49] PA Davidson, F Boysan. The importance of secondary flow in the rotary electromagnetic stirring of steel during continuous casting. *Appl. Sci. Res.*, 44(1987), 241-259.
- [50] C Vives, R Ricou. Fluid flow phenomena in a single phase coreless induction furnace. *Metall. Trans. B*, 16(1985), 227-235.
- [51] D Roger, JF Eastham. Finite element solution of 3D eddy current flow in magnetically linear conductors at power frequencies. *IEEE Trans. Magn.* 18(1982), 481-485.
- [52] RD Pillsbury. A three dimensional eddy current formulation using two potentials: The magnetic vector potential and total scalar potential. *IEEE Trans. Magn.* 19(1983), 2284-2287.
- [53] D Roger, JF Eastham. Multiply connected regions in the A-Y three-dimensional eddy current formulation. *Proc. IEE* 134(1987), 58-66.
- [54] MVK Chari, A Konrad, MA Palmo, J D’Angelo. Three dimensional vector potential analysis for machine field problems. *IEEE Trans. Magn.* 18(1982), 436-446.
- [55] CS Biddlecombe, EA Heighway, J Simkin, CW Trowbridge. Methods for eddy current computation in three dimensions. *IEEE Trans. Magn.* 18(1982), 492-497.

- [56] CJ Carpenter. Comparison of alternative formulations of 3-dimensional magnetic field and eddy-current problems at power frequencies. *Proc. IEE* 124(1977), 1026-1034.
- [57] CJ Carpenter, EA Wyatt. Efficiency of numerical techniques for computing eddy currents in two and three dimensions. *Proc COMPUMAG-76* (1976), 242-250.
- [58] CJ Carpenter, DH Locke. Numerical models of three-dimensional end winding arrays. *Proc. COMPUMAG-76* (1976), 47-55.
- [59] TW Preston, ABJ Reese. Solution of 3-dimensional eddy current problems: The T- Ω method. *IEEE Trans Magn* 18(1982), 486-491.
- [60] W Reinhart, H Stogner, K Pries. Calculation of 3D eddy current problems by finite element method using either an electric or magnetic vector potential. *IEEE Trans. Magn.* 24(1988), 122-125.
- [61] Biro, K Pries. Finite element analysis of 3D eddy currents. *IEEE Trans. Magn.* 26(1990), 418-423.
- [62] JN Reddy. *An Introduction to the Finite Element Method*. (New York: McGraw-Hill, 1993).
- [63] SV Patankar. *Numerical Heat Transfer and Fluid Flow*. (New York: McGraw-Hill, 1980).
- [64] GD Smith. *Numerical Solution of Partial Differential Equations*. (New York: Oxford University Press, 1965).
- [65] SJ Salon. The hybrid finite element-boundary element method in electromagnetics. *IEEE Trans Magn* 21(1985), 1829-1834.
- [66] JL Meyer, N El-Kaddah, J Szekely. A new method for computing electromagnetic force fields in induction furnace. *IEEE Trans Magn* 23(1987), 1806-1810.
- [67] TT Natarajan, N El-Kaddah. A finite element-integral method for two-dimensional eddy current problems. in *Magnetohydrodynamics in Process Metallurgy*. eds J Szekely, JW Evans, K Blazek, N El-Kaddah. (Warrendale, PA: TMS, 1991), 3-9.
- [68] TT Natarajan, N El-Kaddah. Finite element analysis of electromagnetic and fluid flow phenomena in rotary electromagnetic stirring of steel. *Appl. Math. Model.*, 28(2004), 47-61.
- [69] TT Natarajan. An efficient two dimensional FEM/integral method for electromagnetic problems. MS Thesis, University of Alabama, 1991.
- [70] E Kolbe, W Reiss. Eine method zur numerische bestimmung der stromdichteverteilung in inductive erwarmten korpen unterschiedlicher geometrischer form. *Wiss. Z der TH Ilmenau* 9(1963), 311-317.

- [71] RF Dudley, PE Burke. The prediction of current distribution in induction heating installations. *IEEE Trans Industry Applications* 8(1972), 565-571.
- [72] FW Grover. *Inductance Calculations*. (New York: D Van Nostrand, 1946).
- [73] JD Lavers. The influence of system geometry on the electromagnetic stirring forces in crucible induction melting furnaces. in *Metallurgical Applications of Magnetohydrodynamics*. eds HK Moffat, MRE Proctor. (London: The Metals Society, 1984), 62-77.
- [74] JL Meyer, J Szekely, N El-Kaddah. Calculation of the electromagnetic field for induction stirring in continuous casting. *ISIJ Intl.* 27(1987), 25-33.
- [75] N El-Kaddah, J Szekely. The electromagnetic force field, fluid flow field, and temperature profiles in levitated metal droplets. *Metall. Trans. B*, 14(1983), 401-410.
- [76] ERG Eckert, RM Drake. *Analysis of Heat and Mass Transfer*. (New York: McGraw-Hill, 1972).
- [77] TR Goodman. The heat balance integral and its application to problems involving a change in phase. *Trans ASME* 8(1958), 335-342.
- [78] NMH Lightfoot. The solidification of steel ingots. *Proc London Math Soc* 31(1929), 97-116.
- [79] KA Rathjen, LM Jiji. Heat conduction with melting or freezing in a moving corner. *J Heat Transfer* 93(1971), 101-109.
- [80] H Budhia, F Krieth. Heat transfer with melting or freezing in a wedge. *Int J Heat Mass Transfer* 16(1973), 195-211.
- [81] LI Rubinstein. *The Stefan Problem*. (Providence: American Mathematical Society, 1971).
- [82] WD Murray, F Landis. Numerical and machine solutions of transient heat-conduction problems involving melting or freezing. *J Heat Transfer* 81(1959), 106-112.
- [83] SO Unverdi, G Tryggvason. A front-tracking method for viscous, incompressible, multi-fluid flows. *J Comp Phys* 100(1992), 25-37.
- [84] S Osher, JA Sethian. Fronts propagating with curvature-dependent speed: Algorithms based on Hamilton-Jacobi formulations. *J Comp Phys* 79(1988), 12-49.
- [85] J Crank. Two methods for the numerical solution of moving-boundary problems in diffusion and heat flow. *Quart J Mech Appl Math* 10(1957), 220-231.
- [86] JL Duda, MF Malone, RH Notter, JS Vrentas. Analysis of two-dimensional diffusion-controlled moving boundary problems. *Int J Heat Mass Transfer* 18(1975), 901-910.

- [87] T Saitoh. Numerical method for multi-dimensional freezing problems in arbitrary domains. *J Heat Transfer* 100(1978), 294-299.
- [88] CF Hsu, EM Sparrow, SV Patankar. Numerical solution of moving boundary problems by boundary immobilization and a control-volume-based finite-difference scheme. *Int J Heat Mass Transfer* 24(1981), 1335-1343.
- [89] AN Thionov, AA Samarskii. *The Equations of Mathematical Physics, 2nd Ed.* (Moscow: Gittl, 1953).
- [90] J Szekely, NJ Thelemis. *Rate Phenomena in Process Metallurgy.* (New York: Wiley, 1971).
- [91] BM Budak, EN Sobol'eva, AB Uspenskii. A difference method with coefficient smoothing for the solution of Stefan problems. *Zh Vychisl Mat Mat Fiz* (5)(1965), 828-840.
- [92] AA Samarskii, BD Moisyenko. An economic continuous calculation scheme for the Stefan multidimensional problem. *Zh Vychisl Mat Mat Fiz* (5)(1965), 816-827.
- [93] S Chang, DM Stefanescu. A model for macrosegregation and its application to Al-Cu castings. *Met Trans A* 27(1996), 2708-2721
- [94] CA Santos, JA Spim, A Garcia. Modeling of solidification in twin-roll strip casting. *J. Mater. Process. Tech.* 102(2000), 33-39.
- [95] W Oldfield. A qualitative approach to casting solidification. *ASM Trans.* 59(1966), 945-960.
- [96] DM Stefanescu, CS Kanetkar. Modeling of microstructural evolution of eutectic cast iron and of the gray/white transition. *Trans. AFS* 95(1987), 139-144.
- [97] CS Kanetkar, I Chen, DM Stefanescu, N El-Kaddah. A latent heat method for macro-micro modeling of eutectic solidification. *Trans. ISIJ* 28(1988), 860-868.
- [98] O. Budenkova, F. Baltaretu, J. Kovács, A. Roósz, A. Rónaföldi, A.M. Bianchi, and Y. Fautrelle. Simulation of a directional solidification of a binary Al-7wt%Si and a ternary alloy Al-7wt%Si-1wt%Fe under the action of a rotating magnetic field. *Proc. MCWASP XIII, IOP Conference Series: Mater. Sci. Eng.* 33(2012), 012046.
- [99] M Wu, A Fjeld, A Ludwig. Modelling mixed columnar-equiaxed solidification with melt convection and grain sedimentation—Part I: Model description. *Comp. Mater. Sci.* 50(2010), 32-42.
- [100] SA Thorpe, PK Hutt, R Soulsby. The effect of horizontal gradients on thermohaline convection. *J Fluid Mech* 38(1969), 375-400.

- [101] CF Chen. Onset of cellular convection in a salinity gradient due to a lateral temperature gradient. *J Fluid Mech* 63(1974), 563-576.
- [102] ME Thompson, J Szekely. Mathematical and physical modeling of double-diffusive convection of aqueous solutions crystallizing at a vertical wall. *J Fluid Mech* 187(1988), 409-433.
- [103] HE Huppert, MG Worster. Dynamic solidification of a binary melt. *Nature* 314(1985), 367-384.
- [104] W Kurz, DJ Fisher. *Fundamentals of Solidification*. (Rockport, MA: Trans Tech Publications, 1986), 91.
- [105] JA Dantzig, M Rappaz. *Solidification*. (Lausanne: EPFL Press, 2009), 464-466.
- [106] D Brabazon, DJ Browne, AJ Carr. Mechanical stir casting of aluminum alloys from the mushy state: Process, microstructure, and mechanical properties. *Mater. Sci. Eng. A*, 326(2002), 370-381.
- [107] H Puga, JC Teixeira, J Barbosa, E Seabra, S Ribeiro, M Prokic. The combined effect of melt stirring and ultrasonic agitation on the degassing efficiency of AlSi₉Cu₃ alloy. *Mater Lett* 63(2009), 2089-2092.
- [108] AV Kuznetsov. Investigation of the coupled heat transfer, fluid flow, and the solute transport during the strip casting process. *Int J Heat Mass Transfer* 40(1997), 2949-2961.
- [109] N Streat, F Weinberg. Interdendritic fluid flow in a lead-tin alloy. *Met. Trans. B* 7(1976), 417-423.
- [110] R Nasser-Rafi, R Deshmukh, DR Poirier. Flow of interdendritic liquid and permeability in Pb-20wt%Sn alloys. *Met. Mater. Trans. A* 16(1985), 2263-2271.
- [111] R Mehrabian, M Keane, MC Flemings. Interdendritic fluid flow and macrosegregation: Influence of gravity. *Met Trans* 1(1970), 1209-1219.
- [112] J Szekely, AS Jassal. An experimental and analytical study of the solidification of a binary dendritic system. *Met Trans B* 9(1978), 389-397.
- [113] RB Bird, WE Stewart, EN Lightfoot. *Transport Phenomena*. (New York: Wiley, 1960), 196-200.
- [114] RG Santos, MLNM Melo. Permeability of interdendritic channels. *Mater Sci Eng A* 391(2005), 151-158.
- [115] W Shyy, Y Pang, G Hunter, DY Wei, MH Chen. Effect of turbulent heat transfer on continuous ingot solidification. *ASME J. Eng. Mater. Technol.*, 115(1993), 8-16.

- [116] WP Jones, BE Launder. The prediction of laminarization with a two-equation model of turbulence. *Int J Heat Mass Transfer* 15(1972), 301-314.
- [117] H Tennekes, JL Lumley. *A First Course in Turbulence*. (Cambridge, MA: MIT Press, 1972), 19-20.
- [118] R West. On the permeability of the two-phase zone during solidification of alloys. *Met Trans A* 16(1985), 693.
- [119] G Amberg. Computation of macrosegregation in an iron-carbon cast. *Intl. J. Heat Mass Transf.*, 34(1991), 217-227.
- [120] OJ Ilegbusi, MD Mat. Modeling flowability of the mushy zone with a hybrid model utilizing coherency solid fraction. *Mater Sci Eng A* 247(1998), 135-141.
- [121] BE Launder, DB Spalding. *Mathematical Models of Turbulence*. (London, Academic Press, 1972).
- [122] HC Brinkman. A calculation of the viscous force exerted by a flowing fluid on a dense swarm of particles. *Appl. Sci. Res.*, 1(1949), 27-34.
- [123] PG Saffman. On the stability of laminar flow of a dusty gas. *J. Fluid Mech.*, 13(1962), 120-128.
- [124] WT Sproull. Viscosity of dusty gases. *Nature*, 190(1961), 976-978.
- [125] GSF Shire, GL Quarini, TDL Rhys, TS Evans. The anomalous pressure drop behavior of ice slurries flowing through constrictions. *Intl. J. Multiphase Flow*, 34(2008), 510-515.
- [126] Y Yamagishi, H Takeuchi, AT Pyatenko, N Kayakawa. Characteristics of microencapsulated PCM slurry as a heat-transfer fluid. *AIChE J.*, 45(1999), 696-707.
- [127] S Wenji, X Rui, H Chong, H Shihui, D Kaijun, F Ziping. Experimental investigation on TBAB clathrate hydrate slurry flows in a horizontal tube: Forced convective heat transfer behaviors. *Intl. J. Refrig.*, 32(2009), 1801-1807.
- [128] J.L. Alvarado, C. Marsh, C. Sohn, G. Phetteplace, and T. Newell. Thermal performance of microencapsulated phase change material slurry in turbulent flow under constant heat flux. *Intl. J. Heat Mass Transf.*, 50(2007), 1938-1952.
- [129] JS Kirkaldy, WV Youdelis. Contribution to the theory of inverse segregation. *Trans. AIME* 212 (1958), 833-840.
- [130] MC Flemings, GE Nereo. Macrosegregation, Part 1. *AIME Met. Soc. Trans.* 239(1967), 1449-1461.
- [131] KC Chiang and HL Tsai. Shrinkage-induced fluid flow and domain change in two-dimensional alloy solidification. *Intl. J. Heat Mass Transf.*, 35(1992), 1763-1770.

- [132] QZ Diao, HL Tsai. The formation of negative- and positive-segregated bands during solidification of aluminum-copper alloys. *Intl. J. Heat Mass Transf.*, 36(1993), 4299-4305.
- [133] M Rappaz, V Voller. Modeling of micro-macroseggregation in solidification processes. *Metall. Trans. A*, 21(1990), 749-753.
- [134] VR Voller. A numerical scheme for solidification of an alloy. *Canad. Metall. Quart.*, 37 (1998), 169-177.
- [135] VR Voller. On a general back-diffusion parameter. *J. Crystal Growth*, 226(2001), 562-568.
- [136] R Pardeshi, VR Voller, AK Singh, P Dutta. An explicit-implicit time stepping scheme for solidification models. *Intl. J. Heat Mass Transf.*, 51(2008), 3399-3409.